

Turbulent generation of magnetic switchbacks in the Alfvénic solar wind

MUNEHITO SHODA,¹ BENJAMIN D. G. CHANDRAN,² AND STEVEN R. CRANMER³

¹*National Astronomical Observatory of Japan, National Institutes of Natural Sciences, 2-21-1 Osawa, Mitaka, Tokyo, 181-8588, Japan*

²*Department of Physics and Astronomy, University of New Hampshire, Durham, NH 03824, USA*

³*Department of Astrophysical and Planetary Sciences, Laboratory for Atmospheric and Space Physics, University of Colorado, Boulder, CO 80309, USA*

ABSTRACT

One of the most important early results from the *Parker Solar Probe* (PSP) is the ubiquitous presence of magnetic switchbacks, whose origin is under debate. Using a three-dimensional direct numerical simulation of the equations of compressible magnetohydrodynamics from the corona to 40 solar radii, we investigate whether magnetic switchbacks emerge from granulation-driven Alfvén waves and turbulence in the solar wind. The simulated solar wind is an Alfvénic slow-solar-wind stream with a radial profile consistent with various observations, including observations from PSP. As a natural consequence of Alfvén-wave turbulence, the simulation reproduced magnetic switchbacks with many of the same properties as observed switchbacks, including Alfvénic v - b correlation, spherical polarization (low magnetic compressibility), and a volume filling fraction that increases with radial distance. The analysis of propagation speed and scale length shows that the magnetic switchbacks are large-amplitude (nonlinear) Alfvén waves with discontinuities in the magnetic field direction. We directly compare our simulation with observations using a virtual flyby of PSP in our simulation domain. We conclude that at least some of the switchbacks observed by PSP are a natural consequence of the growth in amplitude of spherically polarized Alfvén waves as they propagate away from the Sun.

Keywords: keyword for arXiv submission

1. INTRODUCTION

Low-mass stars on the main-sequence are known to exhibit an intrinsic magnetic field (Saar 2001; Reiners et al. 2009; Vidotto et al. 2014; See et al. 2019) that gives rise to a variety of magnetic activity, including coronal heating (Pizzolato et al. 2003; Ribas et al. 2005; Wright & Drake 2016; Magaúda et al. 2020; Takasao et al. 2020), flares (Maehara et al. 2012; Candelaresi et al. 2014; Davenport 2016; Notsu et al. 2019; Namekata et al. 2020), coronal mass ejections (Cranmer 2017; Moschou et al. 2019; Argiroffi et al. 2019; Maehara et al. 2020), and stellar winds (Wood et al. 2005, 2014). The long-term evolution of stars and planets is strongly affected by this activity: XUV (X-ray + EUV) emission from quiescent coronae and transient flares promote the photo-evaporation of planetary atmospheres (Sanz-Forcada et al. 2011; Johnstone et al. 2019;

Airapetian et al. 2020), while stellar wind can suppress the planetary erosion (Vidotto & Cleary 2020). Stellar angular momentum is extracted by magnetized stellar winds (Weber & Davis 1967; Sakurai 1985; Kawaler 1988; Réville et al. 2015) and/or coronal mass ejections (Aarnio et al. 2012; Jardine et al. 2020), which results in stellar spin-down (Skumanich 1972; Barnes 2003; Irwin & Bouvier 2009; Gallet & Bouvier 2013, 2015; Matt et al. 2015). In fact, the solar wind is observed to transport a significant amount of angular momentum away from the Sun (Finley et al. 2019, 2020a,b). Since only limited and indirect observations are available for stellar winds from other low-mass stars (Wood 2004; Kislyakova et al. 2014; Wood et al. 2014; Vidotto & Bourrier 2017; Jardine & Collier Cameron 2019), theoretical extrapolations from the solar-wind case are often used to infer stellar-wind properties (Cranmer & Saar 2011; Suzuki et al. 2013; Suzuki 2018; Shoda et al. 2020). Further understanding of the solar wind’s formation is becoming increasingly important as a benchmark for stellar-wind modeling.

The classical idea of the solar wind is based on pressure-driven acceleration that leads to a transonic

outflow (Parker 1958, 1965; Velli 1994). Early observation of supersonic plasma velocities in interplanetary space (Neugebauer & Snyder 1962, 1966) supported this idea. This thermally-driven wind model is, however, incomplete in that it cannot reproduce the well-established anti-correlation between solar-wind velocity and coronal (freezing-in) temperature (Geiss et al. 1995; von Steiger et al. 2010) nor the large wind velocities measured in fast-solar-wind streams near earth (Durney 1972). In addition, the solar-wind mass flux remains nearly constant regardless of wind speed or solar activity (Goldstein et al. 1996; Wang 1998; Cohen 2011; Cranmer 2017) in contrast to the thermally-driven model that predicts a sensitive dependence of the mass flux to the coronal temperature (Parker 1965; Lamers & Cassinelli 1999; O’Fionnagáin & Vidotto 2018). To explain these observations, as well as the mass and energy budget across the transition region, a self-consistent description of coronal heating and wind acceleration via magnetic field needs to be considered (Hammer 1982; Withbroe 1988; Hansteen & Leer 1995; Hansteen & Velli 2012). Two different types of magnetically driven solar-wind models have been proposed: wave/turbulence-driven (WTD) models and reconnection/loop-opening (RLO) models (see e.g. Cranmer 2009).

In wave/turbulence-driven models, the solar wind is heated and accelerated by Alfvén waves and turbulence. Alfvén waves are thought to undergo an energy cascade as a consequence of reflection-driven turbulence (Velli et al. 1989; Matthaeus et al. 1999; Dmitruk et al. 2002; Cranmer & van Ballegooijen 2005; Verdini & Velli 2007; Howes & Nielson 2013; Perez & Chandran 2013), phase mixing (Heyvaerts & Priest 1983; Magyar et al. 2017; Magyar & Nakariakov 2020), and/or parametric decay (Sagdeev & Galeev 1969; Goldstein 1978; Derby 1978; Del Zanna et al. 2001; Tenerani & Velli 2013; Chandran 2018; Réville et al. 2018; Shoda et al. 2018b), which results in the observed broadband energy spectrum extending over decades of length and time scales (Coleman 1968; Belcher & Davis 1971; Podesta et al. 2007; Chen et al. 2020). An energy cascade is indeed observed in the solar wind, and the magnitude of the resulting turbulent heating is found to be comparable to what is needed to explain the measured radial profiles of the solar-wind temperature. (Sorriso-Valvo et al. 2007; MacBride et al. 2008; Carbone et al. 2009; Banerjee et al. 2016; Hadid et al. 2017). Alfvén waves also accelerate plasma via the Alfvén-wave-pressure (ponderomotive) force (Dewar 1970; Alazraki & Couturier 1971; Belcher 1971; Jacques 1977). Solar-wind models with Alfvén-wave heating and acceleration are found to self-consistently explain the fast solar wind (Hollweg 1986; Suzuki & Inutsuka 2005;

Cranmer et al. 2007; Verdini et al. 2010; Matsumoto & Suzuki 2012; Lionello et al. 2014; Shoda et al. 2018a; Matsumoto 2020; Sakaue & Shibata 2020), although how turbulence evolves in the solar wind is still under debate (van Ballegooijen & Asgari-Targhi 2016, 2017; Zank et al. 2017; Adhikari et al. 2019; Chandran & Perez 2019; Telloni et al. 2019). In addition, the amplitudes of Alfvén waves in the solar atmosphere appear to be large enough to power the solar wind (De Pontieu et al. 2007; Banerjee et al. 2009; McIntosh et al. 2011; Hahn & Savin 2013; Srivastava et al. 2017). WTD models are also able to reproduce slow solar wind when the super-radial expansion factor of the coronal magnetic field is large (Ofman & Davila 1998; Suzuki & Inutsuka 2006; Cranmer et al. 2007). The global structure of the heliosphere can also be reproduced by WTD models (Usmanov et al. 2011; van der Holst et al. 2014; Usmanov et al. 2018; Réville et al. 2020b).

Compositional analysis of the solar wind indicates that (a part of) the slow solar wind may have a different origin than the fast solar wind. The FIP bias, the degree of relative enhancement of low first-ionization-potential elements, is observed to be large and variable in the slow solar wind (von Steiger et al. 2000; Stansby et al. 2020). A large FIP bias is also observed in closed-loop regions such as helmet streamers (Raymond et al. 1997; Feldman et al. 1998) and active regions (Widing & Feldman 2001; Brooks & Warren 2011; Brooks et al. 2015; Baker et al. 2018; Doschek & Warren 2019), which suggests that slow-solar-wind streams with large FIP bias are formed by the leakage of closed-loop plasma, which is possibly observed as active-region outflows (Sakao et al. 2007; Harra et al. 2008; Brooks & Warren 2011; Brooks et al. 2015) or streamer blobs (Sheeley et al. 1997; Wang et al. 1998; Viall & Vourlidas 2015). Therefore, magnetic reconnection and the resultant opening of loops are possibly central to origin of the slow solar wind. Models of this category are called reconnection/loop-opening (RLO) models (Fisk et al. 1999; Fisk 2003; Antiochos et al. 2011; Higginson et al. 2017; Réville et al. 2020a; Wang 2020). RLO models may be particularly relevant to active stars, for which reconnection and flares occur more frequently.

Winds from coronal holes are believed to be driven by waves and turbulence, because the energy released by magnetic reconnection in coronal holes is likely insufficient to accelerate the solar wind (Cranmer & van Ballegooijen 2010; Lionello et al. 2016). This conclusion, however, is challenged by the *Parker Solar Probe*’s recent observations of large numbers of “magnetic switchbacks” (abrupt, large-angle rotations of the magnetic

field) in solar wind emanating from a low-latitude coronal hole.

Parker Solar Probe (hereafter PSP) (Fox et al. 2016) is a mission to observe the near-Sun solar wind by measuring electromagnetic fields (FIELDS, Bale et al. 2016), the distribution functions of thermal electrons, alpha particles, and protons (SWEAP, Kasper et al. 2016), high-energy particles (IS \odot IS, McComas et al. 2016) and scattered white light (WISPR, Vourlidas et al. 2016). One of the most important early results from PSP is the ubiquitous presence of sudden local magnetic polarity reversal events called magnetic switchbacks (Bale et al. 2019). The presence of switchbacks was first reported in the high-latitude wind (Balogh et al. 1999; Matteini et al. 2014), and later was also found in equatorial wind at 1 au (Gosling et al. 2009) and 0.3 au (Horbury et al. 2018).

The observed properties of switchbacks can be summarized as follows.

1. Switchbacks are usually Alfvénic in the sense that the jump in the magnetic field $\Delta \mathbf{B}$ is associated with a jump in the velocity $\Delta \mathbf{v}$ given by $\pm \Delta \mathbf{B} / \sqrt{4\pi\rho}$, where ρ is the plasma density, and the value of the \pm sign corresponds to Alfvén waves propagating away from the Sun in the local plasma frame. As a consequence, the switchbacks are associated with enhanced values of the radial component of the plasma velocity (Kasper et al. 2019; Bale et al. 2019; Horbury et al. 2020). We note that switchbacks are sometimes observed to have a compressive component (Bale et al. 2019; Farrell et al. 2020).
2. Switchbacks are approximately “spherically polarized,” in the sense that the strength of the magnetic field is almost constant as the field abruptly rotates (Bale et al. 2019; Farrell et al. 2020).
3. Switchbacks appear to be field-aligned, elongated structures with a typical aspect ratio of 10 near the first perihelion (Horbury et al. 2020; Laker et al. 2020).
4. A waiting-time analysis indicates that switchbacks appear in clusters (Dudok de Wit et al. 2020). As a result, although the filling factor of B_r -reversed regions is 6% during PSP’s first perihelion encounter (Bale et al. 2019), the “active phase” of the solar wind that contains switchbacks occupies at least 75% of the total observation time near the first perihelion (Horbury et al. 2020).
5. Switchbacks are S-shaped, locally folded magnetic-field lines. The propagation directions of the elec-

tron strahl (Kasper et al. 2019; Whittlesey et al. 2020), small-scale Alfvén waves (McManus et al. 2020), and proton-alpha differential velocity (Yamauchi et al. 2004b) support this picture.

6. The proton core parallel temperature is found to be constant across switchbacks (Woolley et al. 2020), possibly because switchbacks move through the plasma at the local Alfvén speed, which prevents them from strongly heating any particular parcel of plasma before propagating past it. We note, however, that the active phase mentioned above is characterized by an enhanced proton parallel temperature (Woodham et al. 2020).
7. The volume filling factor of switchbacks is observed to increase as the heliospheric distance increases from $\sim 35R_\odot$ to $\sim 50R_\odot$ (Mozer et al. 2020). In light of the comparative rarity of switchbacks near 1 au, the volume filling factor should begin to decrease somewhere between $50R_\odot$ and 1 au.

The theory of magnetic switchbacks should explain these observational properties.

Possible scenarios for the origin of switchbacks include magnetic transient events (reconnection and/or jets) in the solar atmosphere (Yamauchi et al. 2004a; Roberts et al. 2018; He et al. 2020; Tenerani et al. 2020; Sterling & Moore 2020; Zank et al. 2020), shear-wave interaction (Landi et al. 2006; Ruffolo et al. 2020; Shi et al. 2020) and large-amplitude turbulence (Squire et al. 2020). If magnetic transient events are the principal source of switchbacks, then this would imply that RLO-like events play a significant role even in the coronal-hole wind, which would pose a challenge to the conventional understanding that waves and turbulence dominate the heating and acceleration in coronal-hole wind.

Motivated by the above background, in this work we aim to investigate the theoretical properties of magnetic switchbacks in a wave/turbulence-driven solar-wind model. For this purpose, we perform a three-dimensional direct numerical simulation of the turbulence-driven solar wind from the coronal base to $40R_\odot$, thus directly connecting coronal dynamics and solar-wind fluctuations.

2. MODEL

2.1. Basic equations

We solve the three-dimensional magnetohydrodynamic equations in a local spherical coordinate system that symmetrizes the θ and ϕ directions (Shoda et al. 2019). The ∇ operator in the local spherical coordinate

system is given by

$$\nabla = \mathbf{e}_r \frac{\partial}{\partial r} + \mathbf{e}_\theta \frac{1}{r} \frac{\partial}{\partial \theta} + \mathbf{e}_\phi \frac{1}{r} \frac{\partial}{\partial \phi}, \quad (1)$$

where $\mathbf{e}_{r,\theta,\phi}$ denotes the unit vector in r, θ, ϕ directions. Using Eq. (1), the basic equations are given in the form of a conservation law,

$$\frac{\partial}{\partial t} \mathbf{U} + \frac{1}{r^2} \frac{\partial}{\partial r} (r^2 \mathbf{F}_r) + \frac{1}{r} \frac{\partial}{\partial \theta} \mathbf{F}_\theta + \frac{1}{r} \frac{\partial}{\partial \phi} \mathbf{F}_\phi = \mathbf{S}, \quad (2)$$

where \mathbf{U} , $\mathbf{F}_{r,\theta,\phi}$ and \mathbf{S} are the conserved variables, corresponding fluxes in each direction, and source terms, respectively, which are given by

$$\mathbf{U} = \begin{pmatrix} \rho \\ \rho v_r \\ \rho v_\theta \\ \rho v_\phi \\ \tilde{B}_r \\ \tilde{B}_\theta \\ \tilde{B}_\phi \\ e \\ \zeta \end{pmatrix}, \quad \mathbf{F}_\alpha = \begin{pmatrix} \rho v_\alpha \\ \rho v_\alpha v_r - \tilde{B}_\alpha \tilde{B}_r + p_T \delta_{\alpha,r} \\ \rho v_\alpha v_\theta - \tilde{B}_\alpha \tilde{B}_\theta + p_T \delta_{\alpha,\theta} \\ \rho v_\alpha v_\phi - \tilde{B}_\alpha \tilde{B}_\phi + p_T \delta_{\alpha,\phi} \\ v_\alpha \tilde{B}_r - v_r \tilde{B}_\alpha + \zeta \delta_{\alpha,r} \\ v_\alpha \tilde{B}_\theta - v_\theta \tilde{B}_\alpha + \zeta \delta_{\alpha,\theta} \\ v_\alpha \tilde{B}_\phi - v_\phi \tilde{B}_\alpha + \zeta \delta_{\alpha,\phi} \\ (e + p_T) v_\alpha - \tilde{B}_\alpha (\mathbf{v} \cdot \tilde{\mathbf{B}}) \\ c_h^2 \tilde{B}_\alpha \end{pmatrix}, \quad (3)$$

$$\mathbf{S} = \begin{pmatrix} 0 \\ \rho (v_\theta^2 + v_\phi^2) / r + (2p + \tilde{B}_r^2) / r - \rho g \\ (\tilde{B}_r \tilde{B}_\theta - \rho v_r v_\theta) / r \\ (\tilde{B}_r \tilde{B}_\phi - \rho v_r v_\phi) / r \\ \frac{2\zeta}{r} \\ (v_r \tilde{B}_\theta - v_\theta \tilde{B}_r) / r \\ (v_r \tilde{B}_\phi - v_\phi \tilde{B}_r) / r \\ \rho g v_r + L \\ -\frac{c_h^2}{c_p^2} \zeta \end{pmatrix}, \quad (4)$$

where ζ is the scalar that suppresses numerically generated $\nabla \cdot \mathbf{B}$ (Dedner et al. 2002), $\delta_{\alpha,\beta}$ is the Kronecker delta, $\tilde{\mathbf{B}} = \mathbf{B} / \sqrt{4\pi}$, and \mathbf{B} is the magnetic field. The quantities ρ , \mathbf{v} , e , and p_T are the density, velocity, total energy per unit volume, and total pressure, respectively, the latter two quantities being given by

$$e = \frac{p}{\gamma - 1} + \frac{1}{2} \rho v^2 + \frac{\tilde{B}^2}{2}, \quad p_T = p + \frac{\tilde{B}^2}{2}, \quad (5)$$

where p is the plasma pressure and $\gamma = 5/3$ is the ratio of specific heats. These equations are closed by the

equation of state for a fully-ionized hydrogen plasma:

$$p = 2n_p k_B T, \quad n_p = \rho / m_p, \quad (6)$$

where n_p and m_p are the proton number density and mass, respectively. The quantity g is the gravitational acceleration at a given radial distance,

$$g = \frac{GM_\odot}{r^2} \quad (7)$$

The energy source term L is included to mimic the thermal conduction that works to homogenize the temperature profile. To speed up the simulation, we implement exponential cooling to a given reference temperature profile by setting

$$L = -\frac{1}{\tau_{\text{cnd}}} (e_{\text{int}} - e_{\text{int,ref}}), \quad (8)$$

where $e_{\text{int,ref}}$ is the internal energy corresponding to the reference temperature T_{ref} ,

$$T_{\text{ref}} = T_i \xi_T + T_o (1 - \xi_T), \quad \xi_T = \min \left(1, \frac{1.44}{r/R_\odot} \right), \quad (9)$$

and

$$T_i = 10^6 \text{ K}, \quad T_o = 1.2 \times 10^6 (r/R_\odot)^{-1/2} \text{ K}. \quad (10)$$

We set the relaxation time $\tau_{\text{cnd}} = 1 \text{ s}$ to ensure that the thermal relaxation is faster than the turbulent evolution. Note that this is comparable to the time scale of thermal conduction in the solar wind ($\sim 4 \text{ s}$, assuming a number density of 10^5 cm^{-3} , temperature of 10^6 K , and temperature scale length of 10^5 km).

2.2. Simulation domain and boundary conditions

The simulation domain is a quadrangular pyramid rooted in the coronal base. The range of the simulation domain is defined by $1.02 \leq r/R_\odot \leq 40$, $-\theta_{\text{max}} \leq \theta \leq \theta_{\text{max}}$, $-\phi_{\text{max}} \leq \phi \leq \phi_{\text{max}}$, where $\theta_{\text{max}} = \phi_{\text{max}} = 2.16 \times 10^{-2} \text{ rad}$. The horizontal size of the simulation domain is 30,000 km at the coronal base, which is comparable to the scale of super granulation (Leighton et al. 1962). We employ (16000, 216, 216) uniform grid points in the (r, θ, ϕ) directions.

Periodic boundary conditions are imposed in the θ and ϕ directions. Because the solar wind is supersonic and super-Alfvénic at $r/R_\odot = 40$, free boundary conditions are imposed at the outer boundary. At the inner boundary, fixed boundary conditions are imposed on the density, radial velocity, temperature and radial magnetic field: $\rho_{\text{inner}} = 4.0 \times 10^{-16} \text{ g cm}^{-3}$, $T_{\text{inner}} = 1.0 \times 10^6 \text{ K}$, $v_{r,\text{inner}} = 0.0 \text{ km s}^{-1}$ and $B_{r,\text{inner}} = 1.1 \text{ G}$. The transverse velocity and magnetic field are given in terms of

r/R_\odot	ρ [g cm ⁻³]	v_r [km s ⁻¹]	δv_\perp [km s ⁻¹]	δz_\perp^+ [km s ⁻¹]	δz_\perp^- [km s ⁻¹]	σ_c
1.05	2.92×10^{-16}	0.837	33.5	66.6	2.86	0.996
2.00	2.09×10^{-18}	32.8	88.3	176	5.72	0.998
3.00	3.48×10^{-19}	87.4	121	243	12.0	0.995
5.00	6.23×10^{-20}	175	144	288	26.3	0.984
10.0	9.97×10^{-21}	273	129	258	31.8	0.970
20.0	2.05×10^{-21}	334	92.1	184	22.5	0.971
30.0	8.50×10^{-22}	356	70.6	141	17.5	0.970
39.5	4.42×10^{-22}	373	59.4	120	12.0	0.980

Table 1. Summary of the averaged properties of the simulated solar wind. Columns from left to right stand for radial distance, averaged mass density, averaged radial (wind) velocity, rms perpendicular (wave/turbulence) velocity, rms outward perpendicular Elsässer field, rms inward perpendicular Elsässer field, and normalized cross helicity $\sigma_c = (\delta z_\perp^{+2} - \delta z_\perp^{-2})/(\delta z_\perp^{+2} + \delta z_\perp^{-2})$, respectively.

Elsässer variables defined by

$$z_{\theta,\phi}^\pm = v_{\theta,\phi} \mp \frac{B_{\theta,\phi}}{\sqrt{4\pi\rho}}. \quad (11)$$

To ensure that the velocity and magnetic field are divergence-free below the bottom boundary, the Elsässer variables are given in terms of stream functions.

$$z_{\theta,\text{inner}}^\pm = \frac{1}{r} \frac{\partial}{\partial \phi} \psi_{\text{inner}}^\pm, \quad z_{\phi,\text{inner}}^\pm = -\frac{1}{r} \frac{\partial}{\partial \theta} \psi_{\text{inner}}^\pm. \quad (12)$$

The stream function of the upward component ψ^+ is given such that it has broadband spectra in space and time:

$$\psi_{\text{inner}}^+ \propto \sum_{k_\theta=1}^{n_\theta} \sum_{k_\phi=1}^{n_\phi} \sum_f C(k_\theta, k_\phi, f) \exp \left[2\pi \left(\frac{k_\theta \theta}{2\theta_{\text{max}}} + \frac{k_\phi \phi}{2\phi_{\text{max}}} + ft \right) \right]. \quad (13)$$

Reduced MHD simulations show that the spectral index of upward Elsässer (Alfvén-wave) energy with respect to perpendicular wave number $k_\perp = \sqrt{k_\theta^2 + k_\phi^2}$ is approximately -0.8 at the coronal base, when the perpendicular outer scale of the turbulence in the chromosphere is sufficiently small (see Figure 7 of [Chandran & Perez 2019](#)). Considering this result, the injected Alfvén waves are assumed to exhibit a spectral index of $-2/3$ with respect to k_\perp and a broken power-law spectrum

with respect to f . This is achieved by setting

$$C(k_\theta, k_\phi, f) = k_\perp^{-11/6} / \max \left(1, \sqrt{f/f_{\text{inj}}} \right), \quad (14)$$

which gives a flat frequency spectrum at $f < f_{\text{inj}}$ and a $1/f$ spectrum at $f > f_{\text{inj}}$. We set $n_\theta = n_\phi = 27$ and $f_{\text{inj}} = 10^{-3}$ Hz. The frequency bins in Eq. (13) are uniformly distributed in 10^{-4} Hz $\leq f \leq 10^{-2}$ Hz. The amplitude of ψ^+ is tuned so that the rms amplitude of the velocity fluctuations of the upward Alfvén waves is 30 km s⁻¹ at the lower boundary.

At the lower boundary, the stream function of the downward component is assumed to vanish ($\psi_{\text{inner}}^- = 0$), which yields a discontinuity in the amplitude of the downward Alfvén waves. However, since the amplitude of downward Alfvén waves is small near the bottom boundary ($\lesssim 10$ km s⁻¹), an unphysical discontinuity is unlikely to affect the dynamics of the solar wind.

3. ALFVÉNIC SLOW SOLAR WIND

In approximately 10^5 s, the system reaches a quasi-steady state (QSS) that is not influenced by the initial conditions. Since our interest is the dynamics of turbulence in the quasi-steady solar wind, we analyze the simulation data in the QSS with time duration of $\tau_{\text{dur}} = 1.2 \times 10^4$ s and time cadence of $\Delta t = 6$ s. The actual time step in the simulation is in the order of 10^6 .

In Table 1, we show the averaged properties of the simulated solar wind at several radial distances. The

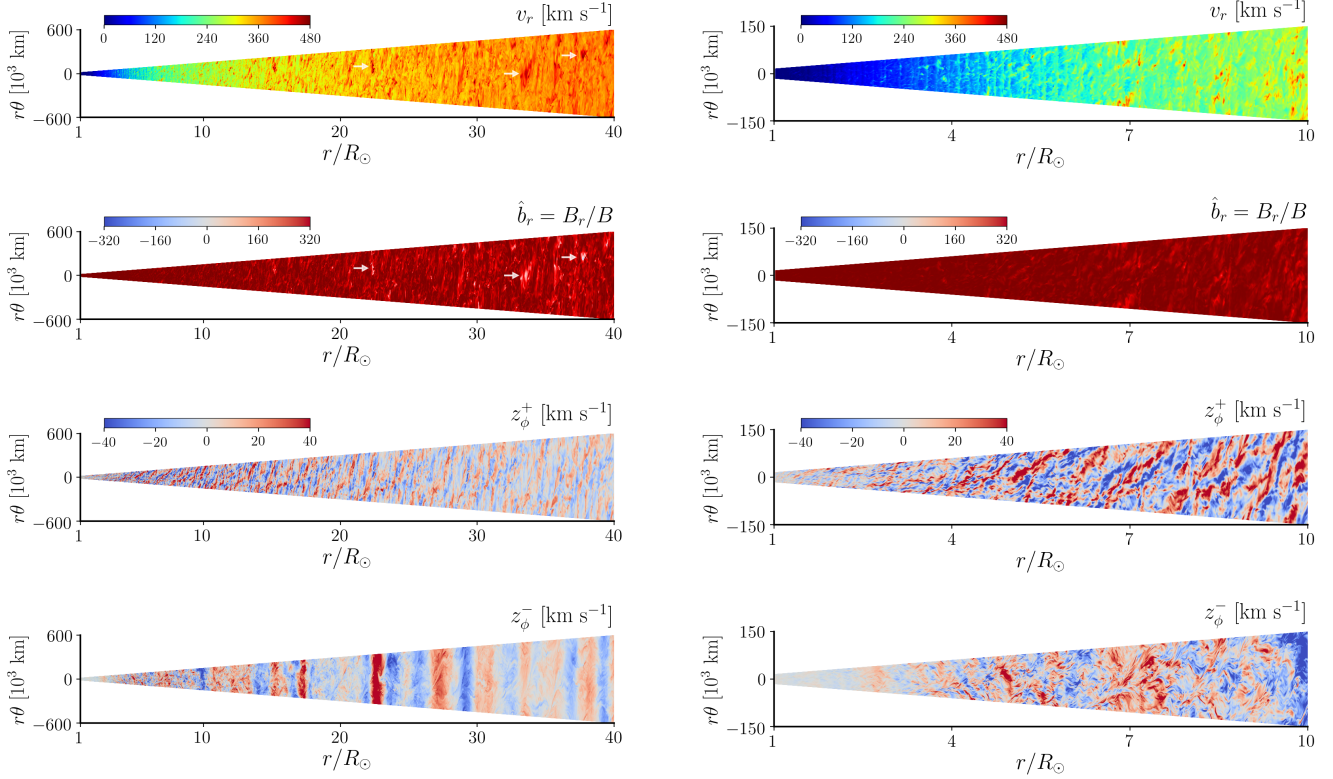


Figure 1. Simulation snapshots in the $r\theta$ plane ($\phi = -\phi_{\max}/2$). Left panels cover the whole simulation domain and the right panels zoom in to the region $1 < r/R_{\odot} < 10$. Note that the vertical axis is scaled up by 200 times for better visualization. Panels from top to bottom show the radial velocity v_r in units of km s^{-1} , normalized radial magnetic field $\hat{b}_r = B_r/B$, ϕ component of outward Elsässer variable z_{ϕ}^{+} in units of km s^{-1} , ϕ component of inward Elsässer variable z_{ϕ}^{-} in units of km s^{-1} , respectively. Large fluctuations in B_r and associated the velocity enhancements are highlighted by white arrows. An animation of this figure is available in the online journal.

simulated solar wind exhibits an averaged mass-loss rate of $2.4\text{--}2.7 \times 10^{-14} M_{\odot} \text{ yr}^{-1}$ (which is in the observed range of $2\text{--}3 \times 10^{-14} M_{\odot} \text{ yr}^{-1}$, see Figure 1 of [Cranmer et al. 2017](#)) and is characterized by its relatively low speed $v_r \lesssim 400 \text{ km s}^{-1}$ and high normalized cross helicity $\sigma_c \gtrsim 0.95$, and thus is categorized as Alfvénic slow solar wind ([Marsch et al. 1981](#); [D’Amicis & Bruno 2015](#); [D’Amicis et al. 2019](#)). Since the first perihelion of PSP is dominated by Alfvénic slow solar wind ([Bale et al. 2019](#)), it is worthwhile to compare our simulation results with the encounter-1 observations.

3.1. Overview on $r\theta$ -plane

To see the radial evolution of the solar wind and turbulence therein, visualization of the vertical ($r\theta$) plane is useful. Figure 1 shows a snapshot of the QSS in the $r\theta$ plane. Left and right panels visualize the whole simulation domain ($1 \leq r/R_{\odot} \leq 40$) and the near-Sun region ($1 \leq r/R_{\odot} \leq 10$), respectively.

The panels that display the outward and inward Elsässer variables show the complex nature of turbu-

lent transport in the solar wind. Comparing the spatial structure of z_{ϕ}^{+} and z_{ϕ}^{-} at $1 < r/R_{\odot} < 10$, one finds finer structures in z_{ϕ}^{-} . This structure difference was previously found in a numerical simulation of fast solar wind ([Shoda et al. 2019](#)). Farther from the sun where the solar wind is super Alfvénic, the chaotic nature of z_{ϕ}^{-} disappears, and instead large-scale structure with respect to θ is evident.

Local reversals of the radial magnetic field are highlighted by arrows in the map of B_r/B . In the near-Sun solar wind, the radial magnetic field is found to exhibit small fluctuations. Beyond $r \sim 25R_{\odot}$, B_r occasionally locally reverses to form magnetic switchbacks ([Bale et al. 2019](#)). Figure 1 also shows that large fluctuations in B_r are associated with local enhancements in v_r , which are also highlighted by arrows. These switchbacks are discussed in more detail in Section 4.

3.2. Radial profiles of the mean field

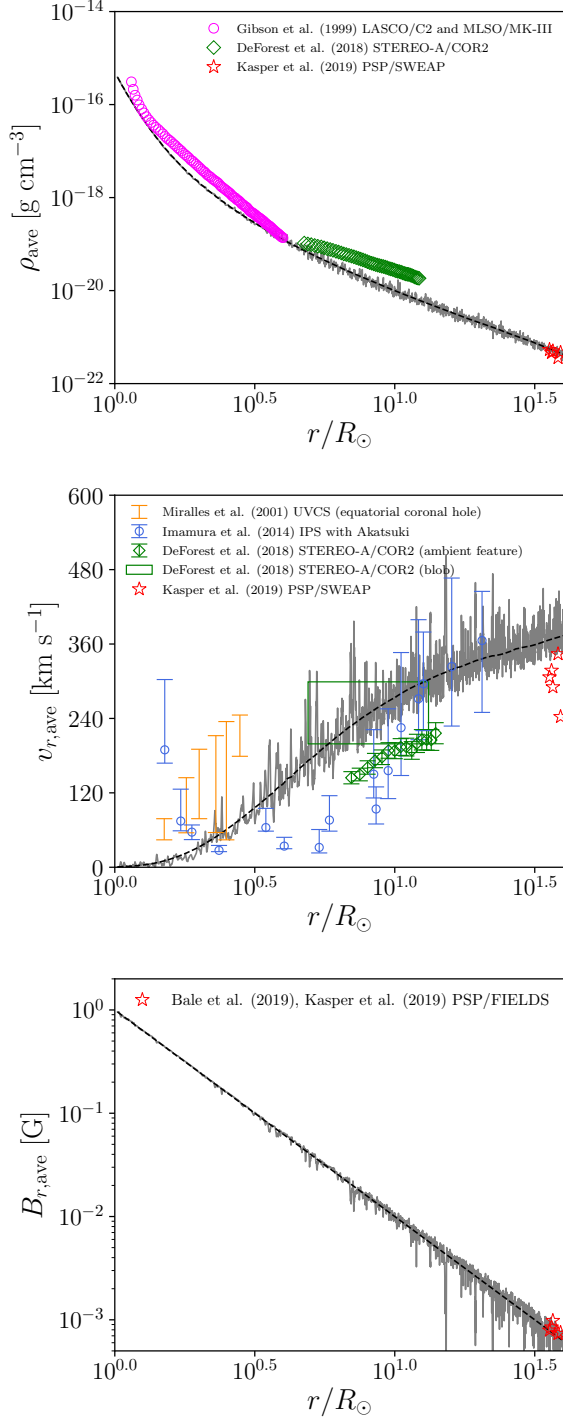


Figure 2. Radial profiles of the mass density (top), radial velocity (middle) and radial magnetic field (bottom). Black dashed and grey solid lines represent averaged and non-averaged (snapshot) profiles, respectively. Symbols show the observed data from Gibson et al. (1999) (pink circles), DeForest et al. (2018) (green diamonds and rectangle), Kasper et al. (2019) (red stars), Miralles et al. (2001) (orange bars), Imamura et al. (2014) (blue circles).

To analyze the large-scale properties of the simulated solar wind, we average the plasma properties and magnetic field over the $\theta\phi$ plane and time. For any given variable X , its horizontal average is defined by

$$\bar{X} \equiv \frac{1}{4\theta_{\text{max}}\phi_{\text{max}}} \int_{-\theta_{\text{max}}}^{\theta_{\text{max}}} d\theta \int_{-\phi_{\text{max}}}^{\phi_{\text{max}}} d\phi X, \quad (15)$$

while its time average is by

$$\langle X \rangle \equiv \frac{1}{\tau_{\text{dur}}} \int_{t_0}^{t_0 + \tau_{\text{dur}}} dt X, \quad (16)$$

where t_0 is the time when the system reached QSS. The averaging time τ_{dur} is set to 1.2×10^4 s. The average with respect to time and horizontal space is denoted by

$$X_{\text{ave}} \equiv \overline{\langle X \rangle}. \quad (17)$$

The root-mean-square fluctuation amplitude of X , δX_{rms} , is defined by

$$\delta X_{\text{rms}} \equiv \sqrt{\langle X^2 \rangle - \langle X \rangle^2}. \quad (18)$$

The black dashed lines in Figure 2 show the radial profiles of the averaged density ρ_{ave} , radial velocity $v_{r,\text{ave}}$, and radial magnetic field $B_{r,\text{ave}}$. Also shown in the grey solid lines are the corresponding non-averaged (snapshot) profiles at the center of the simulation domain ($\theta = \phi = 0$). Observations from SOHO/LASCO (Brueckner et al. 1995), SOHO/UVCS (Kohl et al. 1995, 1997), MLSO/MK-III, STEREO-A/SECCHI/COR2 (Howard et al. 2008), Akatsuki (Nakamura et al. 2011), PSP/FIELDS (Bale et al. 2016), PSP/SWEAP (Kasper et al. 2016) are also plotted (see caption for corresponding papers). All PSP data are retrieved from Kasper et al. (2019) as the most probable values at given radial distance in PSP’s encounter 1. In converting the proton/electron number density to the mass density, we assumed that the helium-to-proton ratio is 5% in number. We note that, although the typical slow solar wind is found to exhibit smaller helium abundance ($\sim 2.5\%$, Kasper et al. 2007), highly Alfvénic slow solar wind can be helium-rich with abundance as large as 5% (Huang et al. 2020).

Although there are broad similarities between our simulation and the observations, there are also several differences. In the density plot, the measurements from DeForest et al. (2018) systematically lie above our model possibly because they estimated the density of blobs while our model shows the density of the ambient solar wind. A systematic gap also exists between our model and the velocity measurements from Miralles et al. (2001). A possible reason for this discrepancy is

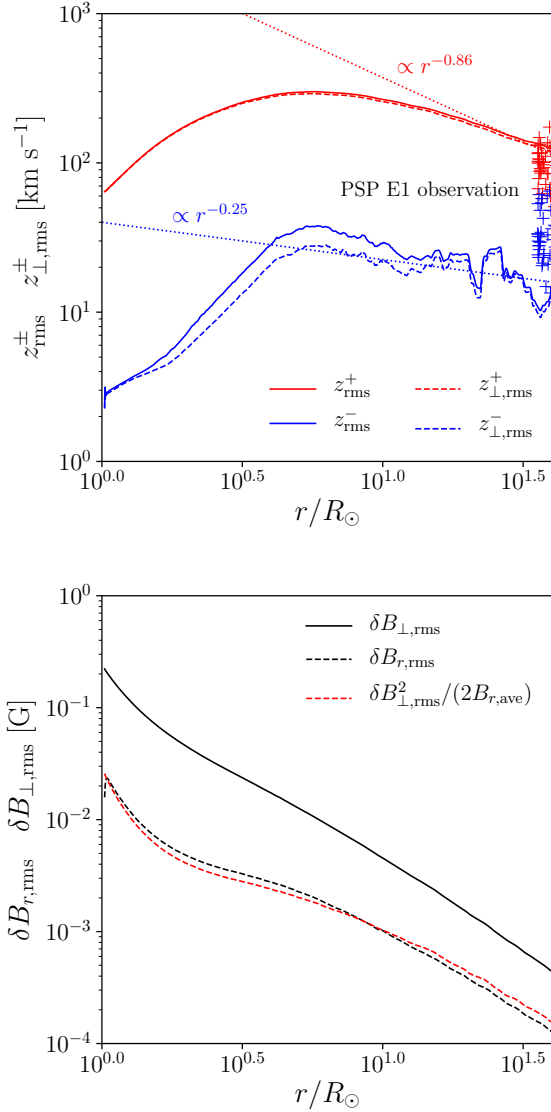


Figure 3. Radial profiles of Elsässer fields and magnetic field. (top) The red and blue lines in the top panel show the rms amplitudes of outward (z^+) and inward (z^-) Elsässer fields. Dashed lines are from transverse (θ and ϕ) components only while solid lines are from the full three components. Crosses represent the observed amplitudes of Elsässer fields during PSP encounter 1 (retrieved from [Chen et al. 2020](#)). The asymptotic radial scaling laws are indicated by dotted lines ([Chen et al. 2020](#)). (bottom) Black solid and dashed lines show the rms amplitudes of fluctuations in transverse and radial magnetic field. Also shown by the red dashed line is $\delta B_{\perp,\text{rms}}^2 / (2B_{r,\text{ave}})$, a theoretical expectation of $\delta B_{r,\text{rms}}$ from [Vasquez & Hollweg \(1998\)](#).

that they reported the outflow velocity of O VI which is often found to be systematically larger than the bulk speed of the solar wind ([Kohl et al. 1998](#)).

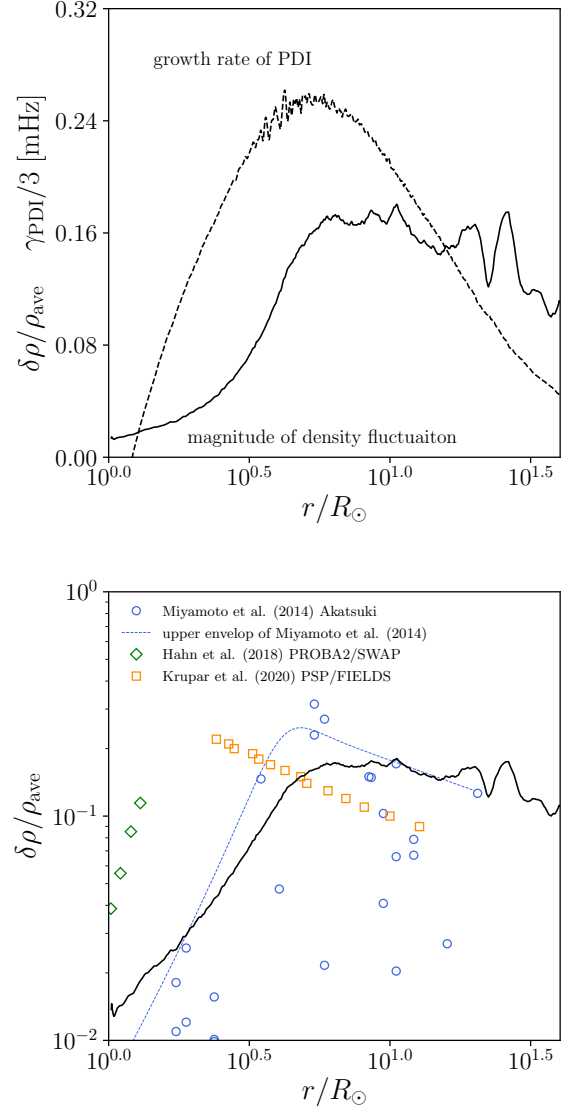


Figure 4. (top) Radial profiles of the fractional density fluctuation $\delta\rho_{\text{rms}}/\rho_{\text{ave}}$ (solid line) and the growth rate of the parametric decay instability (dashed line). (bottom) Comparison of fractional density fluctuations from this model (solid line) and observations (symbols). Symbols represent the observed density fluctuation by Akatsuki (blue circles, [Miyamoto et al. 2014](#)), by PROBA2/SWAP (green diamonds, [Hahn et al. 2018](#)), and by PSP/FIELDS (orange squares, [Krupar et al. 2020](#)).

The radial magnetic field on average scales as $B_r \propto r^{-2}$. This is because the mean field is forced to be aligned with the simulation domain that expands radially in the spherical coordinate system. In the snapshot data (grey line), one finds multiple sudden decreases of B_r (magnetic switchbacks) that appear at $r/R_{\odot} \gtrsim 10$.

3.3. Radial profiles of the fluctuation amplitudes

Since the energy for the wind heating and acceleration lies in the turbulent fluctuations, how the amplitude of the turbulence varies in r is worth investigating. Figure 3 shows the radial profiles of the amplitudes of the fluctuations in the Elsässer fields ($z^\pm = \mathbf{v} \mp \mathbf{B}/\sqrt{4\pi\rho}$) and magnetic field.

In the top panel, solid lines show the rms amplitudes of outward and inward Elsässer fields, and the dashed lines show the rms amplitudes of the transverse components of the Elsässer fields: $z_\perp^\pm = z_\theta^\pm \mathbf{e}_\theta + z_\phi^\pm \mathbf{e}_\phi$. Since the fluctuations are nearly transverse, the solid and dashed lines nearly overlap. Crosses are PSP encounter-1 observations from [Chen et al. \(2020\)](#). Also shown by the dotted lines are asymptotic radial scalings of z^\pm from [Chen et al. \(2020\)](#) (see also [Bavassano et al. 2000](#)). High Alfvénicity is maintained throughout the simulation domain, possibly because the weaker Elsässer field decays more rapidly ([Dobrowolny et al. 1980](#); [Pouquet et al. 1986](#)).

The bottom panel shows the profiles of the radial and transverse magnetic-field fluctuations. The radial-field fluctuation is approximately one order of magnitude smaller than the transverse fluctuation, which is consistent with the transverse nature of the Alfvén wave. According to [Vasquez & Hollweg \(1998\)](#), the interaction between two oblique Alfvén waves with the same group velocity drives a second-order parallel-field fluctuation given by

$$\delta B_\parallel = \frac{1}{2} \frac{B_\perp^2}{B_\parallel}, \quad (19)$$

consistent with earlier work by [Barnes & Hollweg \(1974\)](#) on spherically polarized (or constant- $|\mathbf{B}|$) Alfvén waves. The red dashed line in the bottom panel of Figure 3 shows a root-mean-square version of Eq. (19), which nicely overlaps the black dashed line, supporting the idea that the radial-field fluctuation is driven nonlinearly by oblique Alfvén waves. Eq. (19) predicts that the radial-field fluctuation can be as large as the mean radial field when the Alfvén-wave fluctuation is comparable to the mean field.

In contrast to most reduced-MHD simulations (e.g. [Dmitruk & Matthaeus 2003](#); [van Ballegooijen et al. 2011](#); [Perez & Chandran 2013](#); [Chandran & Perez 2019](#)), our compressible-MHD simulation includes density fluctuations that can be compared with observations. The presence of the density fluctuations in the solar wind is confirmed by several types of measurements ([Tu & Marsch 1994](#); [Miyamoto et al. 2014](#)). Some theoretical studies have been able to reproduce density fluctuations consistent with observed fluctuations ([Suzuki & Inutsuka 2005](#); [Matsumoto & Suzuki 2012](#); [Shoda et al.](#)

[2018a](#)), which possibly result from the parametric decay instability (PDI) of Alfvén waves ([Tenerani & Velli 2013](#); [Tenerani et al. 2017](#); [Chandran 2018](#); [Réville et al. 2018](#); [Bowen et al. 2018](#); [Shoda et al. 2018b](#)). [Shoda et al. \(2019\)](#) showed that the PDI plays an essential role in driving turbulence in the fast solar wind. However, it is unclear whether the PDI is important also in the Alfvénic slow solar wind. Here, we discuss the origin and role of density fluctuations, following an analysis similar to that of [Shoda et al. \(2019\)](#).

Figure 4 shows the radial profile of the fractional density fluctuation $\delta\rho_{\text{rms}}/\rho_{\text{ave}}$ in our model (black solid lines). The growth rate of the parametric decay instability γ_{PDI} is also shown in the top panel (dashed line). In calculating γ_{PDI} we numerically solved the Goldstein–Derby dispersion relation ([Goldstein 1978](#); [Derby 1978](#)) with frequency $f = f_{\text{inj}} = 10^{-3}$ Hz and added the suppression terms from wind acceleration and expansion ([Tenerani & Velli 2013](#); [Shoda et al. 2018b](#)). Comparing the growth rate of the PDI and the magnitude of density fluctuations, one finds that the density fluctuations grow rapidly where the growth rate of the PDI is large. This spatial correlation supports the idea of density-fluctuation generation by the PDI, consistent with what is found in fast-wind simulations ([Shoda et al. 2018b, 2019](#)).

The bottom panel of Figure 4 compares the root-mean-square amplitudes of the simulated and observed density fluctuations. The observed values are from Aka-tuski ([Nakamura et al. 2011](#)), PROBA2/SWAP ([Berghmans et al. 2006](#); [Seaton et al. 2013](#)) and PSP/FIELDS ([Bale et al. 2016](#)) (see caption for the corresponding papers). Radio scintillation observations from [Miyamoto et al. \(2014\)](#) exhibit a large scatter. To take into account the underestimation of the local density-fluctuation amplitude by the positive-negative cancellation along the line of sight, we focus on the upper envelope of the measurements (the blue dashed line) rather than each value (blue circles). The upper envelope is globally consistent with our model. EUV observations (green diamonds) are systematically higher possibly because we ignore the slow magnetosonic waves from below the transition region ([DeForest & Gurman 1998](#); [Ofman et al. 1999](#); [Kid-die et al. 2012](#)) and also the large cross-field variation in the background density along different magnetic flux tubes that has been inferred from Comet-Lovejoy observations ([Raymond et al. 2014](#)).

Type-III radio burst observations (orange squares) show a similar magnitude but a somewhat different trend at $r/R_\odot < 5$. In spite of these differences, overall, the observations are broadly consistent with our model. We note, however, that MHD simulations may overesti-

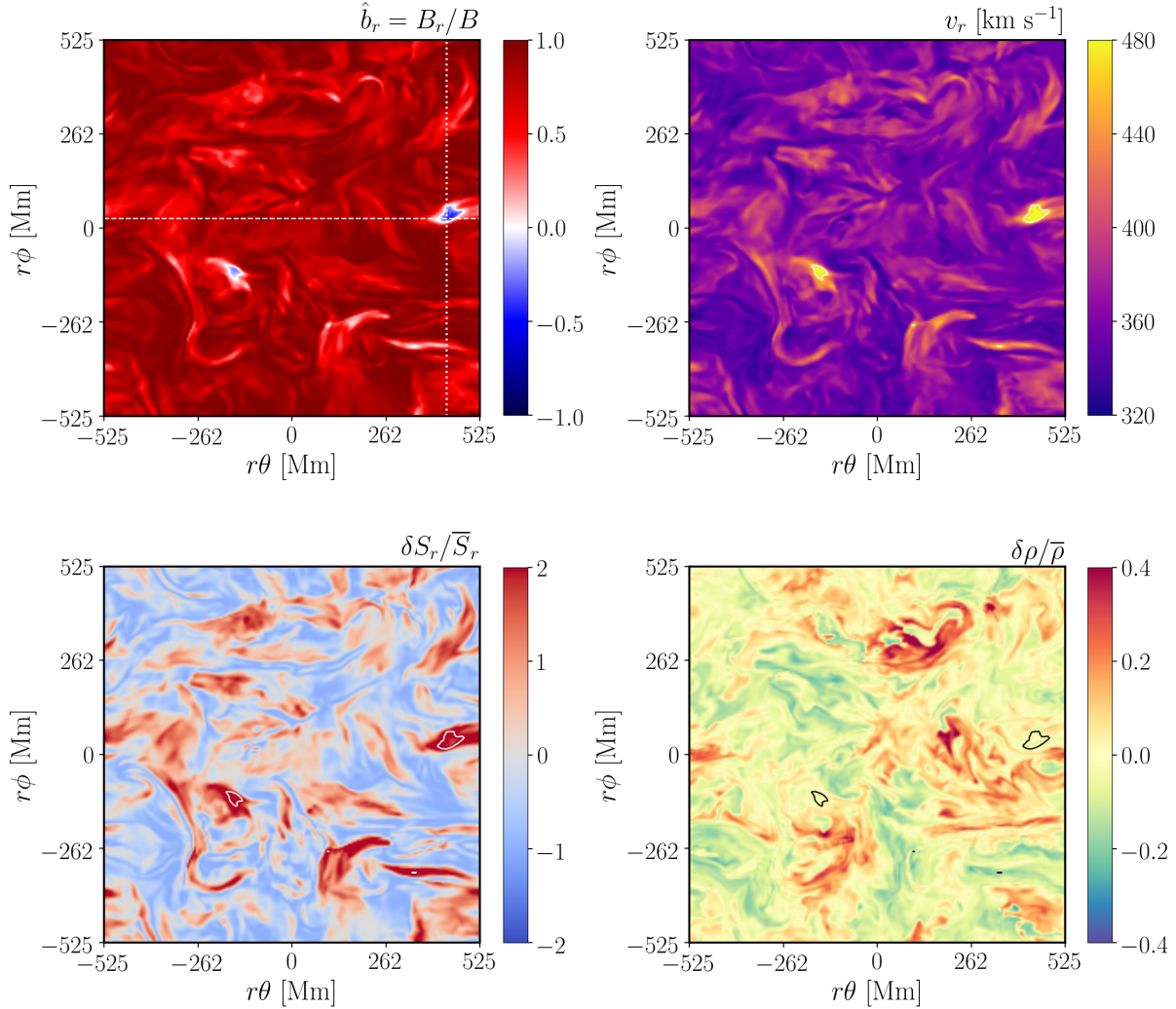


Figure 5. Horizontal ($\theta\phi$ -plane) slice of the simulation domain at $r/R_\odot = 35$. The four panels show the normalized radial magnetic field (B_r/B , top left), radial velocity in unit of km s^{-1} (top right), normalized fluctuation in radial Poynting flux ($\delta S_r/\overline{S_r} = S_r/\overline{S_r} - 1$, bottom left), normalized fluctuation in density ($\delta\rho/\overline{\rho} = \rho/\overline{\rho} - 1$, bottom right), respectively. The white or black solid line corresponds to the boundary of switchbacks: $B_r = 0$. An animation of this figure is available in the online journal.

mate the density fluctuations because they neglect collisionless damping (Barnes 1966; but see Schekhochihin et al 2016, Meyrand et al 2019), and thus care needs to be taken in the interpretation. We also note that fast-mode waves (Cranmer & van Ballegoijen 2012) and co-rotating interaction regions (Cranmer et al. 2013) may also contribute to the observed density fluctuations.

4. MAGNETIC SWITCHBACKS

Figure 1 and the animation of it show the presence of local polarity reversals, i.e., magnetic switchbacks. This section is dedicated to the detailed analysis of switchbacks, focusing on their physical properties and comparing the simulation results with observations. In this

section, magnetic switchbacks are defined as regions in which $B_r < 0$, and switchback boundaries are defined as surfaces on which $B_r = 0$.

4.1. Structure in the $\theta\phi$ plane

To see the localized nature of magnetic switchbacks, we show in Figure 5 the simulation data in the $\theta\phi$ plane at $r/R_\odot = 35$. The four panels show the normalized radial magnetic field B_r/B , density fluctuation $\delta\rho/\overline{\rho} = \rho/\overline{\rho} - 1$, radial Poynting-flux fluctuation $\delta S_r/\overline{S_r} = S_r/\overline{S_r} - 1$, and radial velocity v_r . The white solid lines in the top-right and lower-left panels and the black solid lines in the lower-right panel correspond to the boundaries of magnetic switchbacks (where

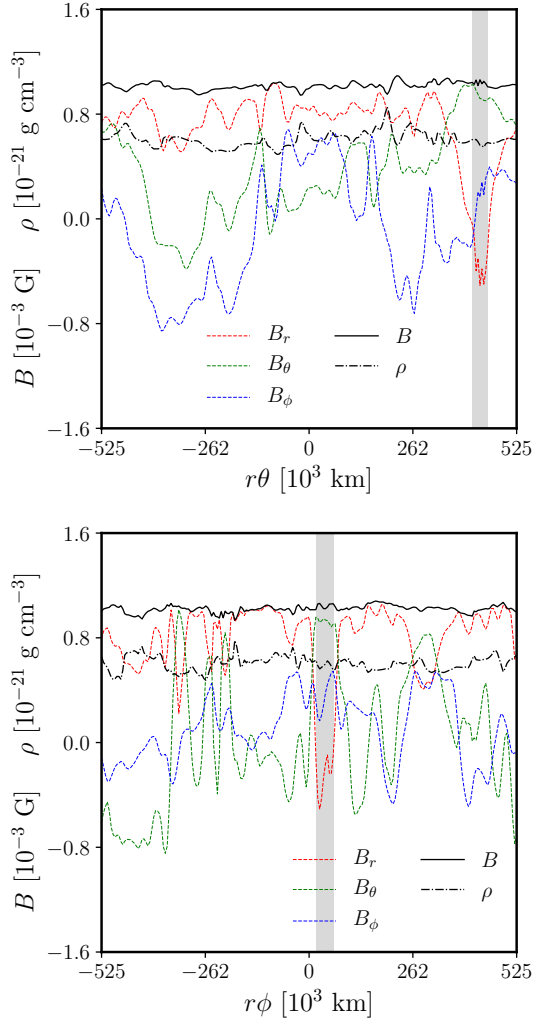


Figure 6. An example of the one-dimensional structure of a magnetic switchback at $r/R_\odot = 35$. The profiles along the dashed and dotted lines in Figure 5 are displayed in the top and bottom panels, respectively, where the switchback region is highlighted by the shaded rectangle.

$B_r = 0$). Note that the overline denotes an average in the $\theta\phi$ plane.

A careful observation of the $\theta\phi$ -plane structure reveals several physical properties of the switchbacks:

1. The switchbacks are highly-localized structures in that their horizontal spatial extent is much smaller than the energy-containing scale of the turbulence, which is comparable to the size of simulation domain in the θ and ϕ directions.
2. The switchbacks are always associated with enhancements in radial velocity and radial Poynting flux. Meanwhile, there does not appear to be any correlation between the emergence of switchbacks and density fluctuations.

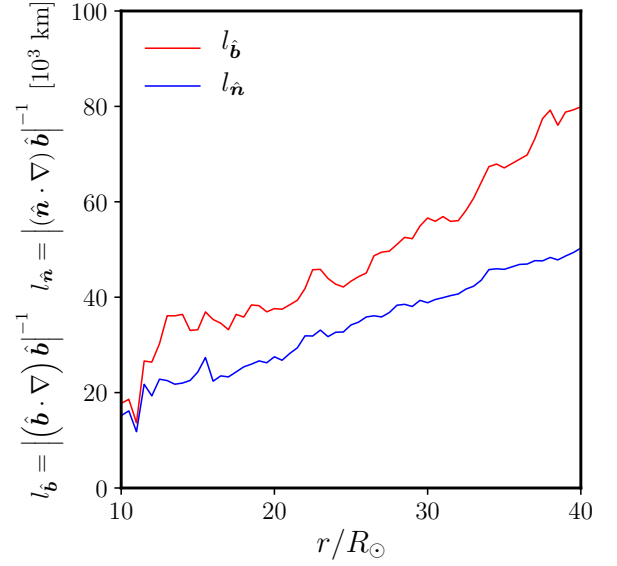


Figure 7. Radial variation of statistically averaged $l_{\hat{\mathbf{b}}}$ (red line) and $l_{\hat{\mathbf{n}}}$ (blue line).

These characteristics are more quantitatively discussed in the following sections.

The structure of a magnetic switchback can be clearly seen in a plot of its one-dimensional spatial profile. Figure 6 shows an example of the one-dimensional structure of a switchback along the white dashed and dotted lines in the left-top panel of Figure 5. An interesting point is that the total magnetic field is nearly constant across the switchback in both the θ and ϕ directions. Another interesting behavior (which is especially clear in the bottom panel) is that the rapid decrease in the B_r component is compensated for by the rapid increase in the perpendicular component B_\perp (B_θ in the bottom panel) while the parallel component B_\parallel (B_ϕ in the bottom panel) is nearly constant. The variation in B_r and B_\perp is larger than the variation of B_\parallel .

To investigate whether switchbacks are closer to rotational discontinuities or tangential discontinuities (see, e.g., Horbury et al. 2001), we define the field-aligned and field-normal length scales (Squire et al. 2020)

$$l_{\hat{\mathbf{b}}} = \left| \left(\hat{\mathbf{b}} \cdot \nabla \right) \hat{\mathbf{b}} \right|^{-1} \quad l_{\hat{\mathbf{n}}} = \left| \left(\hat{\mathbf{n}} \cdot \nabla \right) \hat{\mathbf{b}} \right|^{-1}, \quad (20)$$

where $\hat{\mathbf{b}} = \mathbf{B}/B$ and $\hat{\mathbf{n}}$ is a unit vector normal to $\hat{\mathbf{b}}$ ($\hat{\mathbf{n}} \cdot \hat{\mathbf{b}} = 0$). Taking $\hat{\mathbf{n}}$ to be in the $\theta\phi$ plane, at each given radial distance, $l_{\hat{\mathbf{b}}}$ and $l_{\hat{\mathbf{n}}}$ are calculated at the boundaries of switchbacks (where $B_r = 0$) and then averaged over. To be specific, the total number of detected boundaries is 192 at $r/R_\odot = 10$ and 155002 at $r/R_\odot = 40$.

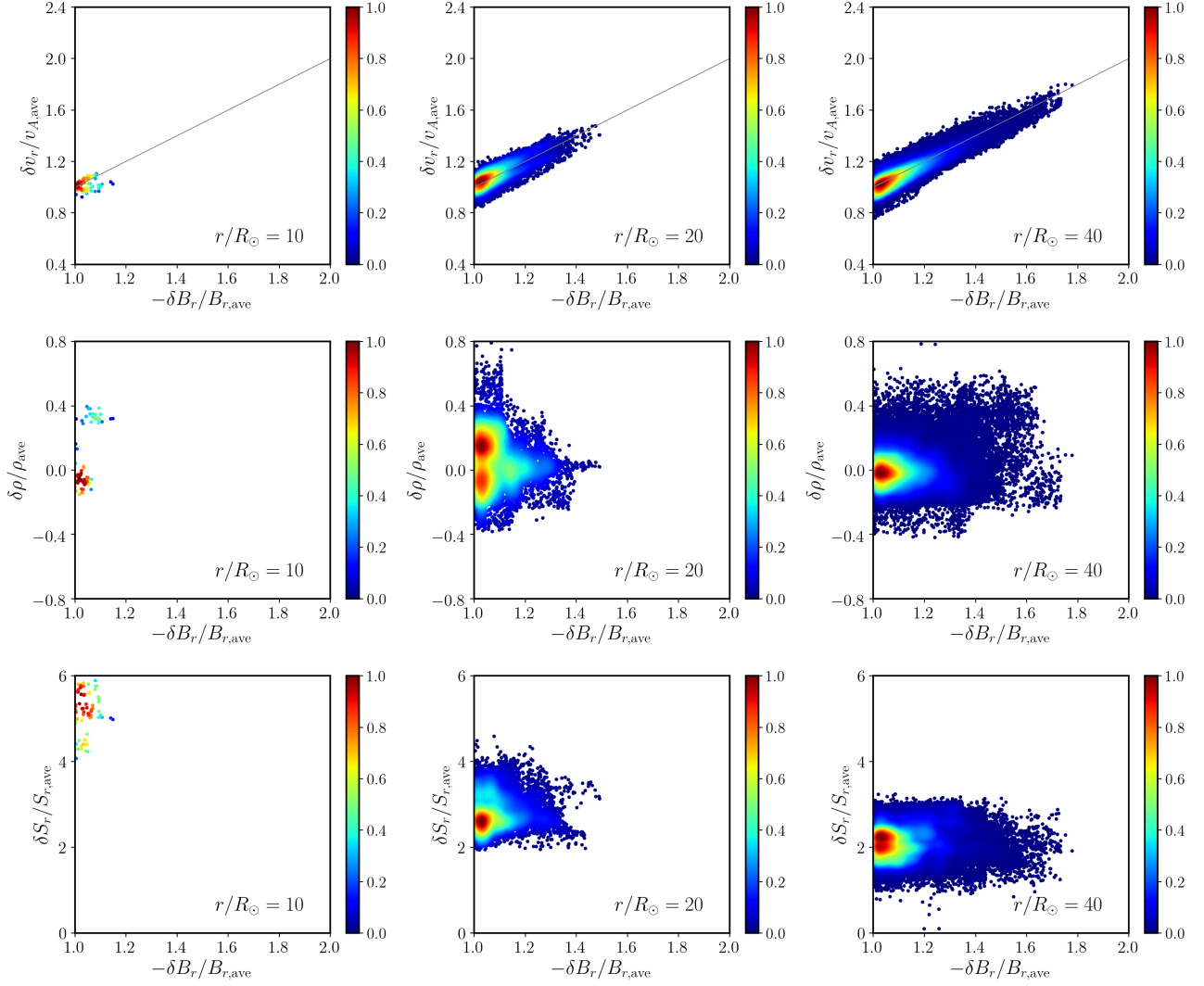


Figure 8. Scatter plots of the normalized radial-field fluctuation $\delta B_r/B_{r,\text{ave}}$ and radial-velocity enhancement ($\delta v_r/v_{Ar,\text{ave}}$, top panels), density fluctuation ($\delta \rho/\rho_{\text{ave}}$, middle panels), and Poynting-flux fluctuation ($\delta S_r/S_{r,\text{ave}}$, bottom panels). Left, center and right panels correspond to $r/R_\odot = 10, 20$, and 40 , respectively. The color represents the normalized kernel density estimate of the points. Grey lines in the top panels show the Alfvénic-correlation relation $\delta B_r/B_{r,\text{ave}} = -\delta v_r/v_{Ar,\text{ave}}$.

The quantities $l_{\hat{\mathbf{b}}}$ and $l_{\hat{\mathbf{n}}}$ represent the length scales of the field deflection in the parallel and perpendicular directions. If the boundary of a switchback is TD-like, the maximum-variation direction is nearly perpendicular, which yields $l_{\hat{\mathbf{b}}} > l_{\hat{\mathbf{n}}}$. The radial variations of averaged $l_{\hat{\mathbf{b}}}$ and $l_{\hat{\mathbf{n}}}$ are shown in the bottom panel of Figure 7. The field-aligned length scale $l_{\hat{\mathbf{b}}}$ is found to be statistically larger than the field-normal length scale $l_{\hat{\mathbf{n}}}$. We thus conclude that switchbacks are on average more TD-like than RD-like.

4.2. Alfvénic nature

Important physical properties of magnetic switchbacks can be inferred from the correlations between their magnetic fluctuations and other quantities. One of the

important correlations is found between the radial-field fluctuation δB_r and the radial-velocity fluctuation δv_r , which are connected by the following Alfvénic relation:

$$\delta B_r/B_{r,\text{ave}} \approx -\delta v_r/v_{Ar,\text{ave}}, \quad (21)$$

where $B_{r,\text{ave}}$ and $v_{Ar,\text{ave}}$ are the averaged radial magnetic field and radial Alfvén speed $v_{Ar} = B_r/\sqrt{4\pi\rho}$. In addition to the radial velocity enhancement, some of the observed magnetic switchbacks are associated with density and Poynting-flux enhancements (Bale et al. 2019). Here we investigate whether these correlations are found in our simulation.

Figure 8 shows scatter plots of normalized B_r fluctuations ($\delta B_r/B_{r,\text{ave}}$) and normalized radial-velocity enhancements $\delta v_r/v_{Ar,\text{ave}}$ (top panels), normalized den-

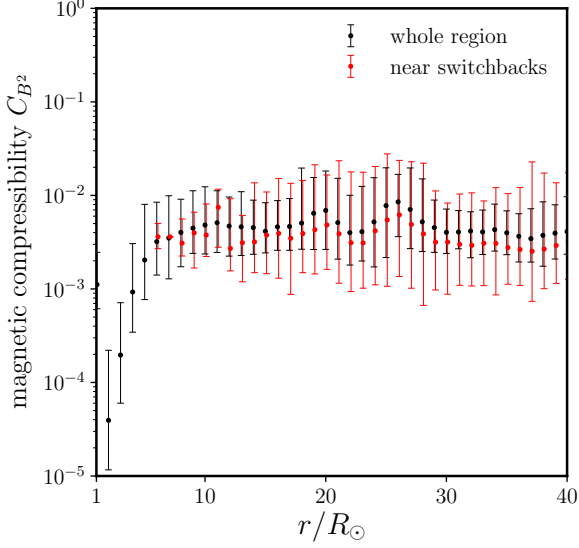


Figure 9. Radial trend of magnetic compressibility C_{B^2} . Upper and lower ends of bar represent the maximum and minimum values and the point indicates the averaged value. Black bars and points are obtained from $\theta\phi$ -plane average while red bars and points are from local average near switchbacks.

sity fluctuations $\delta\rho/\bar{\rho}$ (middle panels), and normalized Poynting-flux fluctuations $\delta S_r/\bar{S}_r$ (bottom panels) at different radial distances, with the color scale indicating the probability of finding each combination of variables in the simulation domain. The grey lines in the top panels show the Alfvénic relation, Eq. (21). Note that the data shown in Figure 8 is restricted to switchback regions in which $\delta B_r + B_{r,\text{ave}} < 0$. Several features are found in these scatter plots:

1. Fluctuations in the radial magnetic field are always associated with fluctuations in the radial velocity. All the switchback events approximately satisfy the Alfvénic relation, Eq. (21), indicating the Alfvénic nature of magnetic switchbacks.
2. No clear correlations are found between density fluctuations and switchbacks, in that the majority of switchback events lie near $\delta\rho = 0$, regardless of the switchback amplitude $\delta B_r/B_{r,\text{ave}}$.
3. Magnetic switchbacks always exhibit larger-than-average Poynting flux. At the same time, within the switchback population, the switchback amplitude is not correlated with the magnitude of the Poynting-flux fluctuation. This means that switchbacks with arbitrary amplitude can emerge once the radial Poynting flux exceeds a critical

threshold value that depends on heliocentric distance.

These results indicate that the switchbacks in our simulation are associated with large-amplitude, unidirectional Alfvén waves that exhibit strong v - B correlation, weak density fluctuations, and larger-than-average radial Poynting flux.

4.3. Magnetic compressibility

The constant- B nature of switchbacks found in Figure 6 is more quantitatively seen from the magnetic compressibility, which is given by

$$C_{B^2} = \left(\frac{\delta |\mathbf{B}|}{|\delta \mathbf{B}|} \right)^2 = \frac{\overline{|B - \bar{B}|^2}}{\overline{|\mathbf{B} - \bar{\mathbf{B}}|^2}}, \quad (22)$$

where $B = |\mathbf{B}|$ and the overline denotes a spatial average.

Black and red symbols in Figure 9 show the radial evolution of magnetic compressibility in the whole $\theta\phi$ plane and near switchbacks (in the square region $[-\theta_{\text{max}}/4 \leq \theta \leq \theta_{\text{max}}/4] \times [-\phi_{\text{max}}/4 \leq \phi \leq \phi_{\text{max}}/4]$ centered at the local minimum of B_r), respectively. The magnetic compressibility is calculated at each time step and thus has a range of values corresponding to different times. The upper and lower ends of the bars show the maximum and minimum values of C_{B^2} , respectively, and the points represent the mean values. The magnetic compressibility defined in the whole $\theta\phi$ -plane is much smaller than unity which is consistent with observations in Alfvénic solar wind. Interestingly, the magnetic compressibility near switchbacks is similar to or even smaller than that defined in the whole $\theta\phi$ plane. In terms of B , this analysis shows that the switchbacks are approximately “spherically polarized,” in the sense of having nearly constant B , consistent with many of the switchbacks observed by PSP.

Some of the observed switchbacks, on the other hand, have a compressional nature. If we define “compressional events” as having $C_{B^2} > 0.02$, then ~ 0.1 – 1% of switchbacks are compressional, which is much smaller than the observed fraction ($\sim 27\%$, see Larosa et al. 2020). Our results suggest that the explanation of such compressional switchbacks lies beyond the mechanisms seen in the simulations presented here and requires additional physics.

4.4. Aspect ratio

PSP measurements suggest that switchbacks are elongated along the background magnetic field, with a typical aspect ratio of 10 (Horbury et al. 2020; Laker et al.

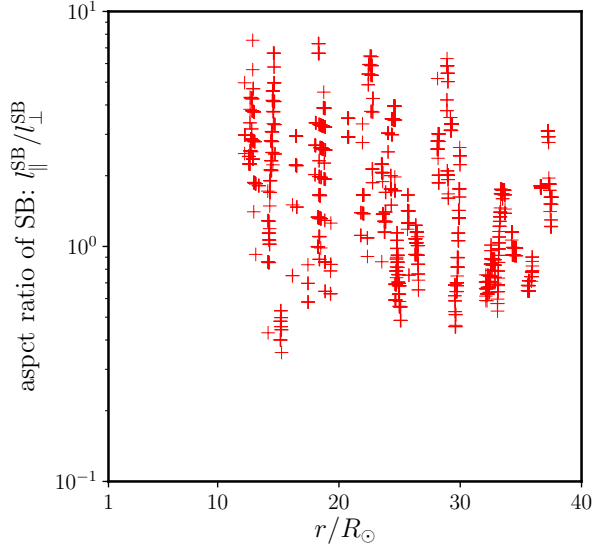


Figure 10. Aspect ratio of the magnetic switchbacks as a function of radial distance. Each point in the figure corresponds to one snapshot.

2020). It is worth investigating whether this large aspect ratio is reproduced in our simulation. We used the following method to measure the aspect ratio of magnetic switchbacks. First, at each time step, we find the minimum- B_r grid point in a given $r\theta$ plane. When the minimum B_r is negative, we define the minimum- B_r point as a switchback region. For each point in a switchback region, the adjacent grid points that satisfy $B_r < 0$ are iteratively found and collectively defined as the switchback region. In this way, we obtain a certain connected domain that satisfies $B_r < 0$ everywhere. The ratio between the radial extent $l_{\parallel}^{\text{SB}}$ and transverse extent l_{\perp}^{SB} of the domain is defined as the aspect ratio: $l_{\parallel}^{\text{SB}}/l_{\perp}^{\text{SB}}$. We note that multiple switchbacks can be found at given ϕ and t , among which we only focus on the one with minimum B_r .

Figure 10 shows the measured aspect ratio as a function of radial distance. Although the data are highly scattered, on average the aspect ratio is larger than unity, indicating elongated structure along the mean-field direction (r axis). The aspect ratio also seems to decrease with r . However, we need to note that the value of aspect ratio is highly influenced by numerical resolution. Most of the switchbacks are resolved by a few grid points in the perpendicular (θ and ϕ) directions and thus are broadened by numerical dissipation. That the aspect ratio is smaller than the typical observed value (~ 10) is possibly due to insufficient resolution. The actual value of the aspect ratio should be investigated in future high-resolution simulations.

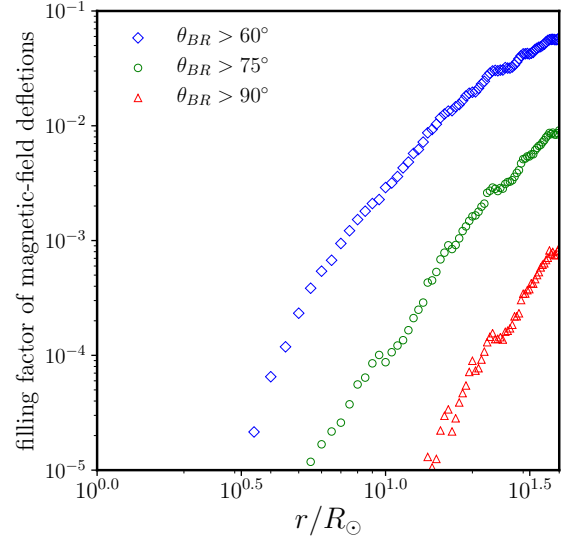


Figure 11. Filling factor of field deflection events versus radial distance. Blue, green and red symbols correspond to the threshold angles of $\theta_{BR} = 60^\circ$, $\theta_{BR} = 75^\circ$, and $\theta_{BR} = 90^\circ$, respectively.

4.5. Filling factor and amplitude histogram

The number of field-deflection events is found to increase with distance from the Sun regardless of the deflection angle (see Figure 3 of Mozer et al. 2020). This trend is observed in our simulation data. To show this, we define the filling factor of field-deflection events via the following procedure. We first count the number of grid points that satisfy the criteria $\theta_{BR} > 60^\circ$, $\theta_{BR} > 75^\circ$, and $\theta_{BR} > 90^\circ$, where θ_{BR} is the angle between the radial direction and the local magnetic field, in each $\theta\phi$ plane over the 2000 time steps we analyze. The filling factor of each field-deflection event is then defined as a ratio of the cumulative counts to the total number of $\theta\phi$ -plane grid points over 2000 steps ($216 \times 216 \times 2000 = 93,312,000$). Figure 11 shows the radial evolution of the filling factors of field-deflection events with $\theta_{BR} > 60^\circ$ (blue), $\theta_{BR} > 75^\circ$ (green), and $\theta_{BR} > 90^\circ$ (red). Regardless of the deflection-angle threshold, the filling factor of field-deflection events increases with radial distance. We note, however, that the filling factor of magnetic switchbacks ($\theta_{BR} > 90^\circ$) is much smaller than the observed value at $r \approx 35R_\odot$ ($\sim 6\%$, see Bale et al. 2019).

The smaller filling factor of switchbacks in our simulation may be due to insufficient resolution. Squire et al. (2020) showed that the number of switchbacks is sensitive to the numerical resolution. In their expanding-box simulations, which are designed to emulate the evolution of Alfvénic turbulence out to $r = 35.7R_\odot$, the switch-

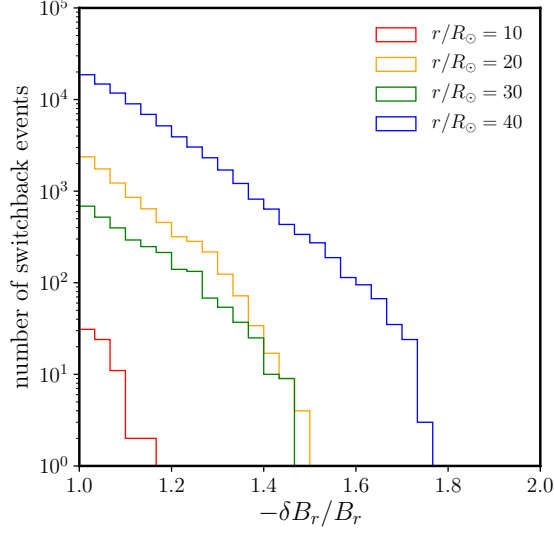


Figure 12. Histogram of normalized switchback amplitudes at four radial distances ($r/R_\odot = 10, 20, 30, 40$).

back filling fraction reaches over 3% in their highest-resolution run, which has 540×1120^2 grid points. In our simulations, if we reduce the resolution of the $\theta\phi$ plane from (216, 216) to (96, 96), the filling factor of magnetic switchbacks is reduced by a factor of 10. Thus, it is possible that the filling factor of magnetic switchbacks would become comparable to the observed value in a higher-resolution version of the simulation we have presented.

The distribution of switchback amplitudes is also of interest. Figure 12 shows histograms of detected switchback events as functions of normalized switchback amplitude $\delta B_r/B_r$. Here a grid point with negative B_r is counted as a switchback event. As shown by this histogram, as well as the number of events, the maximum amplitudes of switchbacks are found to increase with radial distance.

4.6. Propagation speed of magnetic switchbacks

Since the simulation box extends globally from the coronal base to $40R_\odot$, once a magnetic switchback emerges, we are able to measure its propagation velocity by tracing it. Specifically, we measure how the grid position with minimum B_r moves in time. Although this rough estimation yields only a limited number of switchback detections, the number of detected events is sufficiently large to discuss their statistical properties.

Figure 13 compares the detected switchback velocity v_{SB} with the averaged radial velocity $v_{r,ave}$ (black solid line) and radial velocity plus Alfvén speed $v_{r,ave} + v_{A,ave}$ (black dashed line). Clearly the radial profile of v_{SB} matches $v_{r,ave} + v_{A,ave}$, supporting the idea that mag-

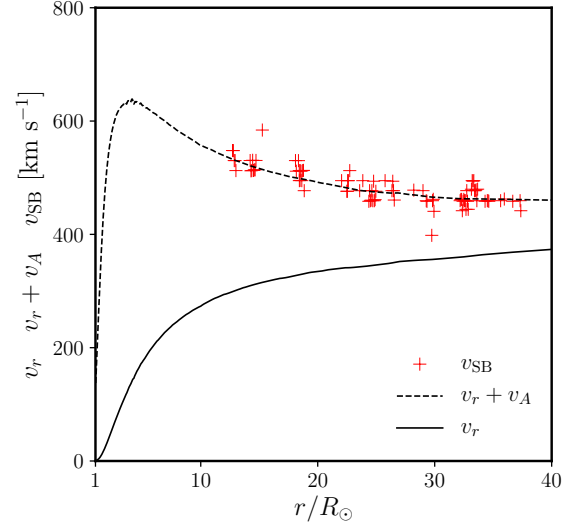


Figure 13. Detected propagation speed of magnetic switchbacks (v_{SB} , red crosses). Black lines are averaged radial velocity ($v_{r,ave}$, solid line) and radial velocity plus Alfvén speed ($v_{r,ave} + v_{A,ave}$, dashed line).

netic switchbacks are locally bent field lines that propagate through the plasma in the anti-Sunward direction at the local Alfvén speed.

5. DIRECT COMPARISON WITH PSP DATA

Since our simulation domain extends beyond the perihelions of *Parker Solar Probe*, a direct comparison between our simulation and PSP observations is possible. Here we compare our simulation results with PSP encounter-1 data.

Around the first perihelion, PSP was nearly co-rotating with the Sun. Although the effect of rotation is not included in our simulation, we simply assume that the simulation domain is co-rotating with the Sun. The location of PSP in the simulation domain is therefore assumed to be fixed in time. For any variable X , the simulated time series of encounter-1 $X_{sim}(t)$ is calculated using the equation

$$X_{sim}(t) = X(r, \theta, \phi, t)|_{r=35.5R_\odot, \theta=-\theta_{max}, \phi=-\phi_{max}}. \quad (23)$$

Observed encounter-1 data of PSP are retrieved from the Coordinated Data Analysis Web (CDAWeb). Magnetic fields in RTN coordinates are taken from the Level-2 data of the fluxgate magnetometer (MAG), part of the FIELDS instrument suite. The proton density and bulk velocity are taken from the Level-3 data of the Solar Probe Cup (SPC), part of the SWEAP instrument

data	B_{ave} [nT]	$B_{r,\text{ave}}$ [nT]	$ \delta \mathbf{B}_{\text{rms}} $ [nT]	$\delta B_{r,\text{rms}}$ [nT]	$\frac{\delta B_{r,\text{rms}}}{ \delta \mathbf{B}_{\text{rms}} }$
observation (12:40–16:00 on 11/05/2018)	81.63	−48.81	62.50	35.76	0.572
observation (6:20–9:40 on 11/06/2018)	86.55	−71.55	47.91	17.44	0.364
simulation	97.20	−79.74	55.42	15.38	0.277

Table 2. This table shows magnetic-field properties in the two observational periods in the encounter 1 and the corresponding simulated data displayed in Figure 14. Note that the averaged and root-mean-squared values are defined in terms of time average over 200 min.

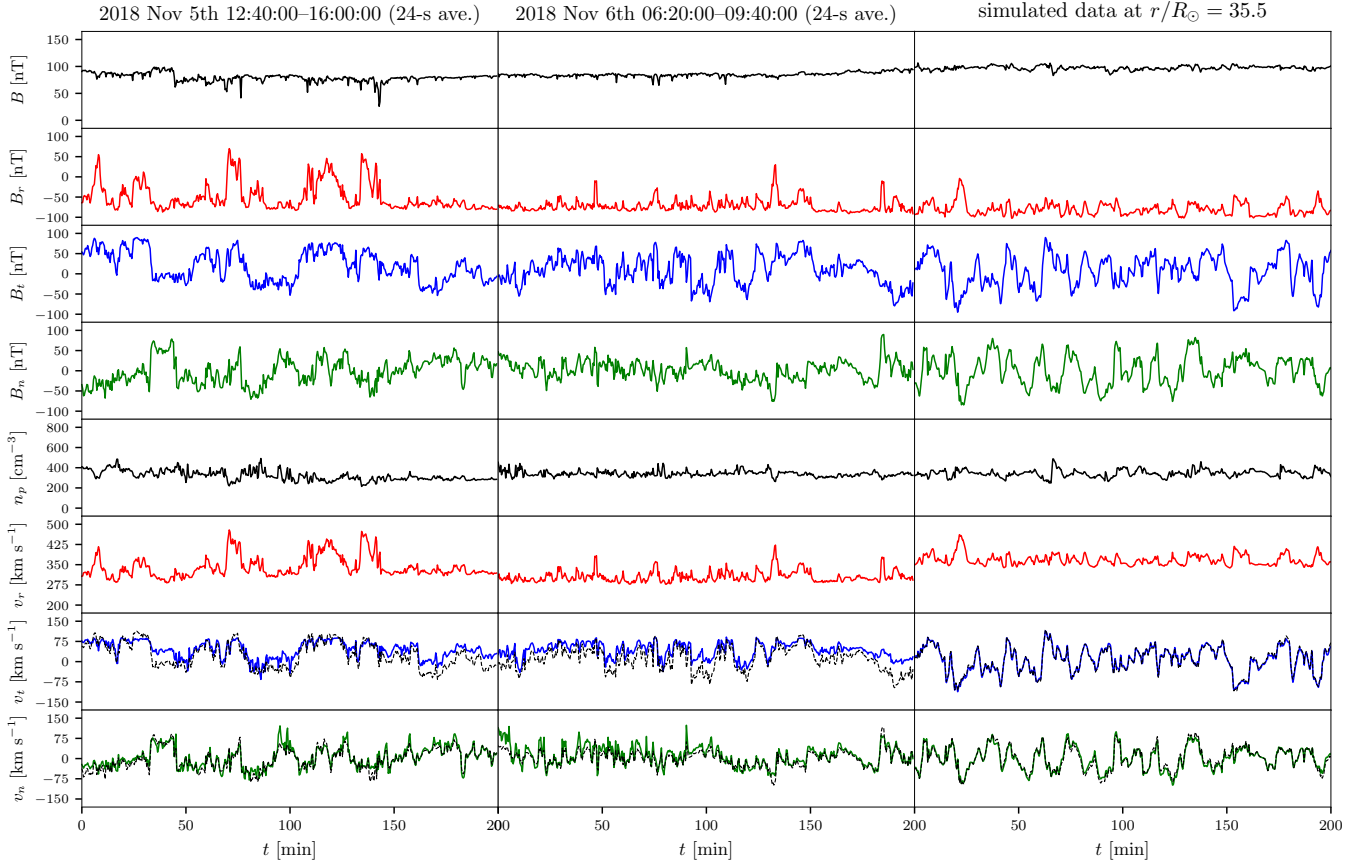


Figure 14. Comparison between PSP data averaged over 24 seconds (left and middle panels) and simulated data retrieved from a virtual PSP flyby through the simulation domain (right panels). Two hundred minutes of data from 12:40 to 16:00 on 2018 November 5th and from 06:20 to 09:40 on 2018 November 6th are shown in the PSP data. The top four panels show magnetic-field data (total field strength B , radial field B_r , tangential field B_t , and normal field B_n) and the bottom four panels show plasma data (proton density n_p , radial velocity v_r , tangential velocity v_t , and normal velocity v_n). Black dashed lines in the bottom two panels show the magnetic field in the Alfvén units: $B_{T,N}/\sqrt{4\pi\rho}$. Magnetic-field data are from MAG/FIELDS and plasma data are from SPC/SWEAP via the Coordinated Data Analysis Web (CDAWeb).

suite, as 0th- and 1st-moments of the reduced distribution function.

Two sets of two-hundred minutes of data are compared with our simulation: the interval from 2018/11/05 12:40:00 to 2018/11/05 16:00:00 and the interval from

2018/11/06 06:20:00 to 2018/11/06 09:40:00. The former period corresponds to a relatively active phase that exhibits large fluctuations in B_r , and the latter to a relatively quiet phase that exhibits small fluctuations in B_r . Table 2 shows the quantitative differ-

ence in the magnetic-field properties in these two periods and the simulated data. The data from Nov 5th are characterized by large $\delta B_{r,\text{rms}}/|\delta \mathbf{B}_{\text{rms}}|$ with little ‘variance anisotropy’: $\delta B_{r,\text{rms}}/|\delta \mathbf{B}_{\text{rms}}| \approx 0.577$ and $\delta B_r \approx \delta B_t \approx \delta B_n$. On the other hand, both the data from Nov 6th and the data from our simulation exhibit much smaller values of $\delta B_{r,\text{rms}}/|\delta \mathbf{B}_{\text{rms}}|$. Since our simulation captures neither high-frequency fluctuations originating from kinetic physics nor sub-grid-scale fluctuations, we take a 24-second time average of the PSP data before comparing with our simulation results.

Figure 14 shows a direct comparison between observed (left and middle column) and simulated data (right column) of PSP. In this comparison, the sign of the simulated magnetic field is changed ($\mathbf{B}_{\text{sim}} \rightarrow -\mathbf{B}_{\text{sim}}$) so that mean magnetic-field polarity is consistent with observations: during this period PSP observed negative-polarity-dominated wind while our simulation assumes a positive-polarity-dominated wind. A change in the sign of \mathbf{B} does not affect the comparison because the structure of field line is invariant. In converting bulk velocity \mathbf{v} to proton bulk velocity \mathbf{v}_p , we assume no differential flow between different species, thus $\mathbf{v} = \mathbf{v}_p$. The proton number density is obtained by a simple assumption that the solar wind is composed of fully ionized hydrogen plasma.

Considering the lack of artificial fine tuning in the simulation, the similarity between the Nov-6th observations and simulation results is surprising. Various observational properties are also seen in the simulated time series: approximately constant density and field strength, the one-sided nature of the fluctuations in v_r and B_r , turbulent fluctuations in \mathbf{v} and \mathbf{B} , and the Alfvénic correlation between \mathbf{B} and \mathbf{v} shown in the bottom two panels of Figure 14.

Meanwhile, the Nov-5th observation exhibits several substantial differences from the simulation data. Magnetic switchbacks that last more than a few minutes are observed multiple times, which are not seen in the simulation data. As a result of the emergence of switchbacks, the magnetic field experiences more discontinuous jumps than the simulation predicts. However, as noted above and shown in Table 2, $\delta B_{r,\text{rms}}/|\delta \mathbf{B}_{\text{rms}}|$ is smaller in the simulation than in the Nov-5 data by a factor of more than 2. Given that the fractional magnetic-field fluctuation is significantly larger in the Nov-5 data, it is perhaps not surprising that switchback features are more prominent than in the simulation. However, it remains to be seen whether a numerical simulation with larger $\delta B_{r,\text{rms}}/|\delta \mathbf{B}_{\text{rms}}|$ (and perhaps higher numerical resolution, as discussed above) could explain the data, or whether additional physical ingredients (such as impul-

sive forcing at the coronal base) are needed. It remains to be seen whether a numerical simulation with higher resolution and/or amplitude could explain the data, or whether additional physical ingredients (such as impulsive forcing at the coronal base) are needed.

6. SUMMARY AND DISCUSSION

In this work, we have performed a direct numerical simulation of the wave/turbulence-driven solar wind. Our simulation yields Alfvénic slow solar wind, the same type of solar wind observed in the first perihelion encounter of PSP. The radial profiles of the density, velocity, and magnetic field are in agreement with remote-sensing observations and in-situ measurements (Figure 2).

The turbulence in our simulations is generated by launching outward-propagating Alfvén waves into our simulation domain through the inner (coronal-base) boundary. These waves become turbulent as they propagate away from the sun and ultimately form magnetic switchbacks. A possible scenario for switchback generation inferred from our simulation is summarized as follows.

1. The normalized amplitude of the Alfvén waves ($\delta B/B$) increases with r due to the expansion of the background flux tube and the decrease of the plasma density (Parker 1965; Heinemann & Olbert 1980).
2. Outward-propagating Alfvén waves nonlinearly evolve towards a constant- B or “spherically polarized” state (Cohen & Kulsrud 1974; Barnes & Hollweg 1974; Vasquez & Hollweg 1998).
3. Once $\delta B/B$ increases to values ~ 1 , the ongoing nonlinear drive towards spherical polarization generates discontinuities in the field, because it is (or at least appears to be) impossible to form a 3D state with constant- B and $\delta B/B \sim 1$ (Barnes 1976; Valentini et al. 2019).

The switchbacks in the simulation have several of the properties exhibited by observed switchbacks, including spherical polarization (Figures 6, 9), Alfvénic v - b correlation (Figure 8), and a volume filling factor that increases with r (Figure 11). Switchbacks are also found to exhibit a rapid change in field direction (Figure 6), to be more ‘TD-like’ than ‘RD-like’ (Figure 7), and to propagate outward at the Alfvén speed in the frame of background flow (Figure 13). From the simulation results and the discussion above, we conclude that at least some of the magnetic switchbacks seen in the solar wind arise as a natural consequence of Alfvén waves and

turbulence with sufficiently large amplitude. However, the volume filling fraction of switchbacks in our simulation is almost two orders of magnitude smaller than in PSP’s first perihelion encounter with the Sun, possibly because of insufficient numerical resolution and/or the fact that $\delta B_{r,\text{rms}}/|\delta \mathbf{B}_{\text{rms}}|$ is smaller in our simulation than in the PSP data (see Table 2). Determining the volume filling fraction in simulations with higher-resolution and different values of $\delta B_{r,\text{rms}}/|\delta \mathbf{B}_{\text{rms}}|$ is an important goal for future research in this area.

In addition to its importance for determining the switchback volume filling factor, running simulations with larger numerical resolution will be important for describing the fine-scale structure of switchbacks, including the local reversal of the cross helicity (McManus et al. 2020). Besides increasing the numerical resolution, there are a number of other ways that the simulation presented here could be further improved. Since an artificial energy source term is used, our model does not accurately capture the thermodynamic properties of switchbacks (Woolley et al. 2020; Woodham et al. 2020). Field-aligned thermal conduction needs to be considered in the future, ideally incorporating the deviation from the Spitzer-Härm heat flux in the weakly collisional, large-Knudsen-number regime (Salem et al. 2003; Bale et al. 2013; Verscharen et al. 2019). Also, kinetic effects are ignored in our MHD treatment. Considering the scale gap between the typical switchback size and the proton gyroradius, the MHD approximation is likely sufficient for describing the dynamics of switchbacks. However, the temperature is anisotropic

in the solar wind (Hellinger et al. 2006), which can affect Alfvén-wave dynamics (Squire et al. 2016; Tenerani & Velli 2018). A fluid approximation with temperature anisotropy (Chandran et al. 2011; Hirabayashi et al. 2016; Tenerani & Velli 2018) is a possible future generalization of the current simulation.

The authors thank Marco Velli, Kosuke Namekata, Shinsuke Takasao, Jono Squire, Romain Meyrand, Alfred Mallet, Stuart Bale, Justin Kasper, and Tim Horbury for valuable discussions and comments. We acknowledge the NASA Parker Solar Probe Mission and the FIELDS team led by S. Bale and SWEAP team led by J. Kasper for use of data. Parker Solar Probe was designed, built, and is now operated by the Johns Hopkins Applied Physics Laboratory as part of NASA’s Living with a Star (LWS) program (contract NNN06AA01C). Support from the LWS management and technical team has played a critical role in the success of the Parker Solar Probe mission. Numerical computations were carried out on the Cray XC50 at the Center for Computational Astrophysics, National Astronomical Observatory of Japan. MS is supported by a Grant-in-Aid for Japan Society for the Promotion of Science (JSPS) Fellows and by the NINS program for cross-disciplinary study (grant Nos. 01321802 and 01311904) on Turbulence, Transport, and Heating Dynamics in Laboratory and Solar/Astrophysical Plasmas: “SoLaBo-X.” BC is supported in part by NASA grant NNN06AA01C to the Parker Solar Probe FIELDS Experiment and by NASA grants NNX17AI18G and 80NSSC19K0829.

REFERENCES

- Aarnio, A. N., Matt, S. P., & Stassun, K. G. 2012, *ApJ*, 760, 9
- Adhikari, L., Zank, G. P., & Zhao, L. L. 2019, *ApJ*, 876, 26
- Airapetian, V. S., et al. 2020, *International Journal of Astrobiology*, 19, 136
- Alazraki, G., & Couturier, P. 1971, *A&A*, 13, 380
- Antiochos, S. K., Mikić, Z., Titov, V. S., Lionello, R., & Linker, J. A. 2011, *ApJ*, 731, 112
- Argiroffi, C., et al. 2019, *Nature Astronomy*, 3, 742
- Baker, D., Brooks, D. H., van Driel-Gesztelyi, L., James, A. W., Démoulin, P., Long, D. M., Warren, H. P., & Williams, D. R. 2018, *ApJ*, 856, 71
- Bale, S. D., Pulupa, M., Salem, C., Chen, C. H. K., & Quataert, E. 2013, *ApJ*, 769, L22
- Bale, S. D., et al. 2016, *SSRv*, 204, 49
- . 2019, *Nature*, 576, 237
- Balogh, A., Forsyth, R. J., Lucek, E. A., Horbury, T. S., & Smith, E. J. 1999, *Geophys. Res. Lett.*, 26, 631
- Banerjee, D., Pérez-Suárez, D., & Doyle, J. G. 2009, *A&A*, 501, L15
- Banerjee, S., Hadid, L. Z., Sahraoui, F., & Galtier, S. 2016, *ApJL*, 829, L27
- Barnes, A. 1976, *J. Geophys. Res.*, 81, 281
- Barnes, A., & Hollweg, J. V. 1974, *J. Geophys. Res.*, 79, 2302
- Barnes, S. A. 2003, *ApJ*, 586, 464
- Bavassano, B., Pietropaolo, E., & Bruno, R. 2000, *J. Geophys. Res.*, 105, 15959
- Belcher, J. W. 1971, *ApJ*, 168, 509
- Belcher, J. W., & Davis, Jr., L. 1971, *J. Geophys. Res.*, 76, 3534
- Berghmans, D., et al. 2006, *Advances in Space Research*, 38, 1807

- Bowen, T. A., Badman, S., Hellinger, P., & Bale, S. D. 2018, *ApJL*, 854, L33
- Brooks, D. H., Ugarte-Urra, I., & Warren, H. P. 2015, *Nature Communications*, 6, 5947
- Brooks, D. H., & Warren, H. P. 2011, *ApJL*, 727, L13
- Brueckner, G. E., et al. 1995, *SoPh*, 162, 357
- Candelaresi, S., Hillier, A., Maehara, H., Brandenburg, A., & Shibata, K. 2014, *ApJ*, 792, 67
- Carbone, V., Marino, R., Sorriso-Valvo, L., Noullez, A., & Bruno, R. 2009, *Physical Review Letters*, 103, 061102
- Chandran, B. D. G. 2018, *Journal of Plasma Physics*, 84, 905840106
- Chandran, B. D. G., Dennis, T. J., Quataert, E., & Bale, S. D. 2011, *ApJ*, 743, 197
- Chandran, B. D. G., & Perez, J. C. 2019, *Journal of Plasma Physics*, 85, 905850409
- Chen, C. H. K., et al. 2020, *ApJS*, 246, 53
- Cohen, O. 2011, *MNRAS*, 417, 2592
- Cohen, R. H., & Kulsrud, R. M. 1974, *Physics of Fluids*, 17, 2215
- Coleman, Jr., P. J. 1968, *ApJ*, 153, 371
- Cranmer, S. R. 2009, *Living Reviews in Solar Physics*, 6, 3
- . 2017, *ApJ*, 840, 114
- Cranmer, S. R., Gibson, S. E., & Riley, P. 2017, *SSRv*, 212, 1345
- Cranmer, S. R., & Saar, S. H. 2011, *ApJ*, 741, 54
- Cranmer, S. R., & van Ballegoijen, A. A. 2005, *ApJS*, 156, 265
- . 2010, *ApJ*, 720, 824
- . 2012, *ApJ*, 754, 92
- Cranmer, S. R., van Ballegoijen, A. A., & Edgar, R. J. 2007, *ApJS*, 171, 520
- Cranmer, S. R., van Ballegoijen, A. A., & Woolsey, L. N. 2013, *ApJ*, 767, 125
- D’Amicis, R., & Bruno, R. 2015, *ApJ*, 805, 84
- D’Amicis, R., Matteini, L., & Bruno, R. 2019, *MNRAS*, 483, 4665
- Davenport, J. R. A. 2016, *ApJ*, 829, 23
- De Pontieu, B., et al. 2007, *Science*, 318, 1574
- Dedner, A., Kemm, F., Kröner, D., Munz, C.-D., Schnitzer, T., & Wesenberg, M. 2002, *Journal of Computational Physics*, 175, 645
- DeForest, C. E., & Gurman, J. B. 1998, *ApJL*, 501, L217
- DeForest, C. E., Howard, R. A., Velli, M., Viall, N., & Vourlidas, A. 2018, *ApJ*, 862, 18
- Del Zanna, L., Velli, M., & Londrillo, P. 2001, *A&A*, 367, 705
- Derby, Jr., N. F. 1978, *ApJ*, 224, 1013
- Dewar, R. L. 1970, *Physics of Fluids*, 13, 2710
- Dmitruk, P., & Matthaeus, W. H. 2003, *ApJ*, 597, 1097
- Dmitruk, P., Matthaeus, W. H., Milano, L. J., Oughton, S., Zank, G. P., & Mullan, D. J. 2002, *ApJ*, 575, 571
- Dobrowolny, M., Mangeney, A., & Veltri, P. 1980, *Physical Review Letters*, 45, 144
- Doschek, G. A., & Warren, H. P. 2019, *ApJ*, 884, 158
- Dudok de Wit, T., et al. 2020, *ApJS*, 246, 39
- Durney, B. R. 1972, *J. Geophys. Res.*, 77, 4042
- Farrell, W. M., MacDowall, R. J., Gruesbeck, J. R., Bale, S. D., & Kasper, J. C. 2020, *ApJS*, 249, 28
- Feldman, U., Schühle, U., Widing, K. G., & Laming, J. M. 1998, *ApJ*, 505, 999
- Finley, A. J., Hewitt, A. L., Matt, S. P., Owens, M., Pinto, R. F., & Réville, V. 2019, *ApJL*, 885, L30
- Finley, A. J., et al. 2020a, *arXiv e-prints*, arXiv:2011.00016
- . 2020b, *ApJL*, 902, L4
- Fisk, L. A. 2003, *Journal of Geophysical Research (Space Physics)*, 108, 1157
- Fisk, L. A., Schwadron, N. A., & Zurbuchen, T. H. 1999, *J. Geophys. Res.*, 104, 19765
- Fox, N. J., et al. 2016, *SSRv*, 204, 7
- Gallet, F., & Bouvier, J. 2013, *A&A*, 556, A36
- . 2015, *A&A*, 577, A98
- Geiss, J., Gloeckler, G., & von Steiger, R. 1995, *SSRv*, 72, 49
- Gibson, S. E., Fludra, A., Bagenal, F., Biesscker, D., del Zanna, G., & Bromage, B. 1999, *J. Geophys. Res.*, 104, 9691
- Goldstein, B. E., et al. 1996, *A&A*, 316, 296
- Goldstein, M. L. 1978, *ApJ*, 219, 700
- Gosling, J. T., McComas, D. J., Roberts, D. A., & Skoug, R. M. 2009, *ApJL*, 695, L213
- Hadid, L. Z., Sahraoui, F., & Galtier, S. 2017, *ApJ*, 838, 9
- Hahn, M., D’Huys, E., & Savin, D. W. 2018, *ApJ*, 860, 34
- Hahn, M., & Savin, D. W. 2013, *ApJ*, 776, 78
- Hammer, R. 1982, *ApJ*, 259, 779
- Hansteen, V. H., & Leer, E. 1995, *J. Geophys. Res.*, 100, 21577
- Hansteen, V. H., & Velli, M. 2012, *SSRv*, 172, 89
- Harra, L. K., Sakao, T., Mandrini, C. H., Hara, H., Imada, S., Young, P. R., van Driel-Gesztelyi, L., & Baker, D. 2008, *ApJL*, 676, L147
- He, J., Zhu, X., Yang, L., Hou, C., Duan, D., Zhang, L., & Wang, Y. 2020, *arXiv e-prints*, arXiv:2009.09254
- Heinemann, M., & Olbert, S. 1980, *J. Geophys. Res.*, 85, 1311
- Hellinger, P., Trávníček, P., Kasper, J. C., & Lazarus, A. J. 2006, *Geophys. Res. Lett.*, 33, L09101
- Heyvaerts, J., & Priest, E. R. 1983, *A&A*, 117, 220
- Higginson, A. K., Antiochos, S. K., DeVore, C. R., Wyper, P. F., & Zurbuchen, T. H. 2017, *ApJ*, 837, 113

- Hirabayashi, K., Hoshino, M., & Amano, T. 2016, *Journal of Computational Physics*, 327, 851
- Hollweg, J. V. 1986, *J. Geophys. Res.*, 91, 4111
- Horbury, T. S., Burgess, D., Fränz, M., & Owen, C. J. 2001, *Geophys. Res. Lett.*, 28, 677
- Horbury, T. S., Matteini, L., & Stansby, D. 2018, *MNRAS*, 478, 1980
- Horbury, T. S., et al. 2020, *ApJS*, 246, 45
- Howard, R. A., et al. 2008, *SSRv*, 136, 67
- Howes, G. G., & Nielson, K. D. 2013, *Physics of Plasmas*, 20, 072302
- Huang, J., et al. 2020, arXiv e-prints, arXiv:2005.12372
- Imamura, T., et al. 2014, *ApJ*, 788, 117
- Irwin, J., & Bouvier, J. 2009, in *IAU Symposium*, Vol. 258, *The Ages of Stars*, ed. E. E. Mamajek, D. R. Soderblom, & R. F. G. Wyse, 363–374
- Jacques, S. A. 1977, *ApJ*, 215, 942
- Jardine, M., & Collier Cameron, A. 2019, *MNRAS*, 482, 2853
- Jardine, M., Collier Cameron, A., Donati, J. F., & Hussain, G. A. J. 2020, *MNRAS*, 491, 4076
- Johnstone, C. P., Khodachenko, M. L., Lüftinger, T., Kislyakova, K. G., Lammer, H., & Güdel, M. 2019, *A&A*, 624, L10
- Kasper, J. C., Stevens, M. L., Lazarus, A. J., Steinberg, J. T., & Ogilvie, K. W. 2007, *ApJ*, 660, 901
- Kasper, J. C., et al. 2016, *SSRv*, 204, 131
- . 2019, *Nature*, 576, 228
- Kawaler, S. D. 1988, *ApJ*, 333, 236
- Kiddie, G., De Moortel, I., Del Zanna, G., McIntosh, S. W., & Whittaker, I. 2012, *SoPh*, 279, 427
- Kislyakova, K. G., Holmström, M., Lammer, H., Odert, P., & Khodachenko, M. L. 2014, *Science*, 346, 981
- Kohl, J. L., et al. 1995, *SoPh*, 162, 313
- . 1997, *SoPh*, 175, 613
- . 1998, *ApJL*, 501, L127
- Krupar, V., et al. 2020, *ApJS*, 246, 57
- Laker, R., et al. 2020, arXiv e-prints, arXiv:2010.10211
- Lamers, H. J. G. L. M., & Cassinelli, J. P. 1999, *Introduction to Stellar Winds*, 452
- Landi, S., Hellinger, P., & Velli, M. 2006, *Geophys. Res. Lett.*, 33, L14101
- Larosa, A., et al. 2020, arXiv e-prints, arXiv:2012.10420
- Leighton, R. B., Noyes, R. W., & Simon, G. W. 1962, *ApJ*, 135, 474
- Lionello, R., Török, T., Titov, V. S., Leake, J. E., Mikić, Z., Linker, J. A., & Linton, M. G. 2016, *ApJL*, 831, L2
- Lionello, R., Velli, M., Downs, C., Linker, J. A., Mikić, Z., & Verdini, A. 2014, *ApJ*, 784, 120
- MacBride, B. T., Smith, C. W., & Forman, M. A. 2008, *ApJ*, 679, 1644
- Maehara, H., et al. 2012, *Nature*, 485, 478
- . 2020, *PASJ*
- Magaudda, E., Stelzer, B., Covey, K. R., Raetz, S., Matt, S. P., & Scholz, A. 2020, arXiv e-prints, arXiv:2004.02904
- Magyar, N., & Nakariakov, V. M. 2020, arXiv e-prints, arXiv:2012.00811
- Magyar, N., Van Doorselaere, T., & Goossens, M. 2017, *Scientific Reports*, 7, 14820
- Marsch, E., Rosenbauer, H., Schwenn, R., Muehlhaeuser, K. H., & Denskat, K. U. 1981, *J. Geophys. Res.*, 86, 9199
- Matsumoto, T. 2020, arXiv e-prints, arXiv:2009.03770
- Matsumoto, T., & Suzuki, T. K. 2012, *ApJ*, 749, 8
- Matt, S. P., Brun, A. S., Baraffe, I., Bouvier, J., & Chabrier, G. 2015, *ApJL*, 799, L23
- Matteini, L., Horbury, T. S., Neugebauer, M., & Goldstein, B. E. 2014, *Geophys. Res. Lett.*, 41, 259
- Matthaeus, W. H., Zank, G. P., Oughton, S., Mullan, D. J., & Dmitruk, P. 1999, *ApJL*, 523, L93
- McComas, D. J., et al. 2016, *SSRv*, 204, 187
- McIntosh, S. W., de Pontieu, B., Carlsson, M., Hansteen, V., Boerner, P., & Goossens, M. 2011, *Nature*, 475, 477
- McManus, M. D., et al. 2020, *ApJS*, 246, 67
- Miralles, M. P., Cranmer, S. R., Panasyuk, A. V., Romoli, M., & Kohl, J. L. 2001, *ApJL*, 549, L257
- Miyamoto, M., et al. 2014, *ApJ*, 797, 51
- Moschou, S.-P., Drake, J. J., Cohen, O., Alvarado-Gómez, J. D., Garraffo, C., & Fraschetti, F. 2019, *ApJ*, 877, 105
- Mozer, F. S., et al. 2020, *ApJS*, 246, 68
- Nakamura, M., et al. 2011, *Earth, Planets, and Space*, 63, 443
- Namekata, K., et al. 2020, *PASJ*, 72, 68
- Neugebauer, M., & Snyder, C. W. 1962, *Science*, 138, 1095
- . 1966, *J. Geophys. Res.*, 71, 4469
- Notsu, Y., et al. 2019, *ApJ*, 876, 58
- O’Fionnagáin, D., & Vidotto, A. A. 2018, *MNRAS*, 476, 2465
- Ofman, L., & Davila, J. M. 1998, *J. Geophys. Res.*, 103, 23677
- Ofman, L., Nakariakov, V. M., & DeForest, C. E. 1999, *ApJ*, 514, 441
- Parker, E. N. 1958, *ApJ*, 128, 664
- . 1965, *SSRv*, 4, 666
- Perez, J. C., & Chandran, B. D. G. 2013, *ApJ*, 776, 124
- Pizzolato, N., Maggio, A., Micela, G., Sciortino, S., & Ventura, P. 2003, *A&A*, 397, 147
- Podesta, J. J., Roberts, D. A., & Goldstein, M. L. 2007, *ApJ*, 664, 543

- Pouquet, A., Frisch, U., & Meneguzzi, M. 1986, *PhRvA*, 33, 4266
- Raymond, J. C., McCauley, P. I., Cranmer, S. R., & Downs, C. 2014, *ApJ*, 788, 152
- Raymond, J. C., et al. 1997, *SoPh*, 175, 645
- Reiners, A., Basri, G., & Browning, M. 2009, *ApJ*, 692, 538
- Réville, V., Brun, A. S., Matt, S. P., Strugarek, A., & Pinto, R. F. 2015, *ApJ*, 798, 116
- Réville, V., Tenerani, A., & Velli, M. 2018, *ApJ*, 866, 38
- Réville, V., Velli, M., Rouillard, A. P., Lavraud, B., Tenerani, A., Shi, C., & Strugarek, A. 2020a, *ApJL*, 895, L20
- Réville, V., et al. 2020b, *ApJS*, 246, 24
- Ribas, I., Guinan, E. F., Güdel, M., & Audard, M. 2005, *ApJ*, 622, 680
- Roberts, M. A., Uritsky, V. M., DeVore, C. R., & Karpen, J. T. 2018, *ApJ*, 866, 14
- Ruffolo, D., et al. 2020, *ApJ*, 902, 94
- Saar, S. H. 2001, *Astronomical Society of the Pacific Conference Series*, Vol. 223, *Recent Measurements of (and Inferences About) Magnetic Fields on K and M Stars (CD-ROM Directory: contribs/saar1)*, ed. R. J. Garcia Lopez, R. Rebolo, & M. R. Zapaterio Osorio, 292
- Sagdeev, R. Z., & Galeev, A. A. 1969, *Nonlinear Plasma Theory*
- Sakao, T., et al. 2007, *Science*, 318, 1585
- Sakaue, T., & Shibata, K. 2020, *ApJ*, 900, 120
- Sakurai, T. 1985, *A&A*, 152, 121
- Salem, C., Hubert, D., Lacombe, C., Bale, S. D., Mangeney, A., Larson, D. E., & Lin, R. P. 2003, *ApJ*, 585, 1147
- Sanz-Forcada, J., Micela, G., Ribas, I., Pollock, A. M. T., Eiroa, C., Velasco, A., Solano, E., & García-Álvarez, D. 2011, *A&A*, 532, A6
- Seaton, D. B., et al. 2013, *SoPh*, 286, 43
- See, V., et al. 2019, *ApJ*, 886, 120
- Sheeley, N. R., et al. 1997, *ApJ*, 484, 472
- Shi, C., Velli, M., Tenerani, A., Rappazzo, F., & Réville, V. 2020, *ApJ*, 888, 68
- Shoda, M., Suzuki, T. K., Asgari-Targhi, M., & Yokoyama, T. 2019, *ApJL*, 880, L2
- Shoda, M., Yokoyama, T., & Suzuki, T. K. 2018a, *ApJ*, 853, 190
- . 2018b, *ApJ*, 860, 17
- Shoda, M., et al. 2020, *ApJ*, 896, 123
- Skumanich, A. 1972, *ApJ*, 171, 565
- Sorriso-Valvo, L., et al. 2007, *PhRvL*, 99, 115001
- Squire, J., Chandran, B. D. G., & Meyrand, R. 2020, *ApJL*, 891, L2
- Squire, J., Quataert, E., & Schekochihin, A. A. 2016, *ApJL*, 830, L25
- Srivastava, A. K., et al. 2017, *Scientific Reports*, 7, 43147
- Stansby, D., Baker, D., Brooks, D. H., & Owen, C. J. 2020, *A&A*, 640, A28
- Sterling, A. C., & Moore, R. L. 2020, *ApJL*, 896, L18
- Suzuki, T. K. 2018, *PASJ*, 70, 34
- Suzuki, T. K., Imada, S., Kataoka, R., Kato, Y., Matsumoto, T., Miyahara, H., & Tsuneta, S. 2013, *PASJ*, 65, 98
- Suzuki, T. K., & Inutsuka, S.-i. 2005, *ApJL*, 632, L49
- Suzuki, T. K., & Inutsuka, S.-I. 2006, *Journal of Geophysical Research (Space Physics)*, 111, 6101
- Takasao, S., Mitsuishi, I., Shimura, T., Yoshida, A., Kunitomo, M., Tanaka, Y. A., & Ishihara, D. 2020, *ApJ*, 901, 70
- Telloni, D., Carbone, F., Bruno, R., Sorriso-Valvo, L., Zank, G. P., Adhikari, L., & Hunana, P. 2019, *ApJ*, 887, 160
- Tenerani, A., & Velli, M. 2013, *Journal of Geophysical Research (Space Physics)*, 118, 7507
- . 2018, *ApJL*, 867, L26
- Tenerani, A., Velli, M., & Hellinger, P. 2017, *ApJ*, 851, 99
- Tenerani, A., et al. 2020, *ApJS*, 246, 32
- Tu, C. Y., & Marsch, E. 1994, *J. Geophys. Res.*, 99, 21,481
- Usmanov, A. V., Matthaeus, W. H., Breech, B. A., & Goldstein, M. L. 2011, *ApJ*, 727, 84
- Usmanov, A. V., Matthaeus, W. H., Goldstein, M. L., & Chhiber, R. 2018, *ApJ*, 865, 25
- Valentini, F., Malara, F., Sorriso-Valvo, L., Bruno, R., & Primavera, L. 2019, *ApJL*, 881, L5
- van Ballegooijen, A. A., & Asgari-Targhi, M. 2016, *ApJ*, 821, 106
- . 2017, *ApJ*, 835, 10
- van Ballegooijen, A. A., Asgari-Targhi, M., Cranmer, S. R., & DeLuca, E. E. 2011, *ApJ*, 736, 3
- van der Holst, B., Sokolov, I. V., Meng, X., Jin, M., Manchester, IV, W. B., Tóth, G., & Gombosi, T. I. 2014, *ApJ*, 782, 81
- Vasquez, B. J., & Hollweg, J. V. 1998, *J. Geophys. Res.*, 103, 335
- Velli, M. 1994, *ApJL*, 432, L55
- Velli, M., Grappin, R., & Mangeney, A. 1989, *Physical Review Letters*, 63, 1807
- Verdini, A., & Velli, M. 2007, *ApJ*, 662, 669
- Verdini, A., Velli, M., Matthaeus, W. H., Oughton, S., & Dmitruk, P. 2010, *ApJL*, 708, L116
- Verscharen, D., Klein, K. G., & Maruca, B. A. 2019, *arXiv e-prints*, arXiv:1902.03448
- Viall, N. M., & Vourlidas, A. 2015, *ApJ*, 807, 176
- Vidotto, A. A., & Bourrier, V. 2017, *MNRAS*, 470, 4026
- Vidotto, A. A., & Cleary, A. 2020, *MNRAS*, 494, 2417
- Vidotto, A. A., et al. 2014, *MNRAS*, 441, 2361

- von Steiger, R., Zurbuchen, T. H., & McComas, D. J. 2010, *Geophys. Res. Lett.*, 37, L22101
- von Steiger, R., et al. 2000, *J. Geophys. Res.*, 105, 27217
- Vourlidas, A., et al. 2016, *SSRv*, 204, 83
- Wang, Y. M. 1998, in *Astronomical Society of the Pacific Conference Series*, Vol. 154, *Cool Stars, Stellar Systems, and the Sun*, ed. R. A. Donahue & J. A. Bookbinder, 131
- Wang, Y. M. 2020, *ApJ*, 904, 199
- Wang, Y. M., et al. 1998, *ApJL*, 498, L165
- Weber, E. J., & Davis, Jr., L. 1967, *ApJ*, 148, 217
- Whittlesey, P. L., et al. 2020, *ApJS*, 246, 74
- Widing, K. G., & Feldman, U. 2001, *ApJ*, 555, 426
- Withbroe, G. L. 1988, *ApJ*, 325, 442
- Wood, B. E. 2004, *Living Reviews in Solar Physics*, 1, 2
- Wood, B. E., Müller, H.-R., Redfield, S., & Edelman, E. 2014, *ApJL*, 781, L33
- Wood, B. E., Müller, H. R., Zank, G. P., Linsky, J. L., & Redfield, S. 2005, *ApJL*, 628, L143
- Woodham, L. D., et al. 2020, *arXiv e-prints*, arXiv:2010.10379
- Woolley, T., et al. 2020, *MNRAS*, 498, 5524
- Wright, N. J., & Drake, J. J. 2016, *Nature*, 535, 526
- Yamauchi, Y., Moore, R. L., Suess, S. T., Wang, H., & Sakurai, T. 2004a, *ApJ*, 605, 511
- Yamauchi, Y., Suess, S. T., Steinberg, J. T., & Sakurai, T. 2004b, *Journal of Geophysical Research (Space Physics)*, 109, A03104
- Zank, G. P., Adhikari, L., Hunana, P., Shiota, D., Bruno, R., & Telloni, D. 2017, *ApJ*, 835, 147
- Zank, G. P., Nakanotani, M., Zhao, L. L., Adhikari, L., & Kasper, J. 2020, *ApJ*, 903, 1